

Design and Performance Analysis of AFDM with Multiple Antennas in Doubly Selective Channels

Haoran Yin, *Graduate Student Member, IEEE*, Xizhang Wei, Yanqun Tang, and Kai Yang, *Member, IEEE*

Abstract—On the heels of orthogonal time frequency space (OTFS) modulation, the recently discovered affine frequency division multiplexing (AFDM) is a promising waveform for the sixth-generation wireless network. In this paper, we introduce the multiple-input multiple-output AFDM (MIMO-AFDM) system, which combines the superiorities of high multiplexing and diversity gain from MIMO and strong delay-Doppler spread resilience from AFDM. In the case of ideal channel state information (CSI), we first formulate the vectorized input-output relationship, and then prove that the MIMO-AFDM system can achieve full diversity in doubly selective channels. Consequently, MIMO-AFDM has a bit error ratio (BER) performance identical to MIMO-OTFS while outperforming MIMO-OFDM significantly. Moreover, for the case of imperfect CSI, we propose a low-complexity embedded pilot-aided diagonal reconstruction (EPADR) channel estimation scheme. Simulation results show that MIMO-AFDM with estimated CSI establishes the BER performance similar to that with ideal CSI. Finally, we investigate the orthogonal resource allocation of affine frequency division multiple access (AFDMA) system, which shows great potential for multiple access in high mobility scenarios thanks to its high efficiency and flexibility.

Index Terms—MIMO-AFDM, DAFT domain, doubly selective channels, diversity analysis, channel estimation, AFDMA.

I. INTRODUCTION

THE sixth-generation wireless network is envisioned to provide ultra-reliable, high data rate and low-latency communications in high mobility scenarios, including vehicle-to-vehicle (V2V), unmanned aerial vehicles (UAV), high-speed trains and low-earth-orbit satellite (LEOS), etc. The dynamic channels therein are characterized by heavy delay-Doppler spreads, which cast a huge challenge to the current widely adopted waveforms, such as orthogonal frequency division multiplexing (OFDM) [1], [2]. The non-negligible Doppler shifts greatly devastate the orthogonality between the subcarriers in OFDM [3]–[5], which is a serious problem especially in the case of higher frequency bands used in the future communication systems.

Many efforts have been made to design a new modulation waveform to accommodate time- and frequency-selective channels. In particular, a two-dimensional (2D) modulation waveform named orthogonal time frequency space (OTFS)

has attracted substantial attention [6]–[10]. The main idea of OTFS is multiplexing the information symbols in the delay-Doppler (DD) domain, where a quasi-static channel representation can be obtained. The recent works on OTFS have shown the performance superiority of OTFS over OFDM in single-antenna and multiple-antenna systems [11]–[17]. In [13], the diversity order of multiple-input multiple-output OTFS (MIMO-OTFS) was proven to be the number of receive antennas, and a phase rotation scheme using transcendental numbers was proposed for MIMO-OTFS to extract full diversity order. In [14], an embedded pilot-based channel estimation scheme was proposed for MIMO-OTFS and OTFS multiple access (OTFS-MA) systems. While [18]–[20] investigated the resource allocation schemes for OTFS-MA system. However, a disadvantage of OTFS is the heavy guard symbol overhead when conducting pilot-aided channel estimation due to its 2D structure, especially in the configuration of multiple antennas [21].

Affine frequency division multiplexing (AFDM), a newly discovered waveform, always attains full diversity in doubly selective channels [22]. Information symbols in AFDM are multiplexed on a set of orthogonal chirps via inverse *discrete affine Fourier transform* (DAFT), which is a generalization of the widely adopted inverse *discrete Fourier transform* (DFT) [23]–[25]. It is shown in [22] that the AFDM modulation/demodulation can be implemented efficiently using the OFDM modulator/demodulator as an inner core. Moreover, by tuning the chirp slope according to the Doppler profile of the channel appropriately, AFDM manages to separate the propagation paths with distinct delay or Doppler shifts in the one-dimensional DAFT domain. Hence, similar to OTFS, AFDM can transform a time-variant channel in the time-frequency domain into a quasi-time-invariant channel. The separability, stability and sparsity of the DAFT domain channel representation facilitate the channel estimation and signal detection in AFDM. These unique characteristics distinguish AFDM from another chirp-based waveform named orthogonal chirp division multiplexing (OCDM) [26]. Some recent works have studied the implementation of practical AFDM systems. For example, a pilot-aided path detection based channel estimation scheme was presented in [27], where the Doppler shift of each propagation path was assumed to be the integral multiple of the subcarrier spacing. An embedded pilot-aided approximated maximum likelihood (EPA-AML) channel estimation scheme was proposed for AFDM in [21], where the advantage of AFDM over OTFS on lower channel estimation overhead has been highlighted. Besides, by exploring the diagonal property of the effective channel matrix of AFDM,

This work was supported in part by Guangdong Natural Science Foundation under Grant 2019A1515011622. (*Corresponding author: Yanqun Tang.*)

Haoran Yin, Xizhang Wei and Yanqun Tang are with the School of Electronics and Communication Engineering, Sun Yat-sen University, China (e-mail: yinh6@mail2.sysu.edu.cn, weixzh7@mail.sysu.edu.cn, tangyq8@mail.sysu.edu.cn).

Kai Yang is with the School of Information and Electronics, Beijing Institute of Technology, Beijing, China (email: yangkai@ieee.org).

a weighted maximal-ratio combining based low-complexity iterative decision feedback equalizer and a low-complexity MMSE detector were proposed for AFDM signal detection in [28]. The potential of AFDM for communication at high-frequency bands was presented in [29], showing that AFDM is robust against radio frequency impairments, such as carrier frequency offset and phase noise. The suitability of AFDM for integrated sensing and communications was investigated in [30] and [31]. Simulation results in [21], [22], [28], [29] show that AFDM has a bit error ratio (BER) performance identical to OTFS and outperforms OFDM greatly in doubly selective channels.

While the above works have revealed the superiority of AFDM, they all focus on single-input single-output AFDM (SISO-AFDM) system. To the best of our knowledge, the combinations of AFDM with multiple-antenna techniques, including multiple-input multiple-output AFDM (MIMO-AFDM) and affine frequency division multiple access (AFDMA) systems, have not been studied in the literature. Considering that multiple-antenna techniques will continue to play a crucial role in the sixth-generation wireless network, we fill this gap in the following. Our contributions can be summarized as follows.

- We first develop the settings of MIMO-AFDM system and derive the associated input-output relationship in the DAFT domain. Based on that, we extend the diversity analysis of SISO-AFDM in [21] to MIMO-AFDM with ideal channel state information (CSI). It is shown that MIMO-AFDM can achieve full diversity in doubly selective channels, where the full diversity order refers to the number of receive antennas multiplied by the number of paths that are separable in either delay or Doppler domain. Numerical results validate that, similar to MIMO-OTFS, MIMO-AFDM possesses a BER performance better than MIMO-OFDM.
- Next, based on our previous work in [27], we analyze the diagonal reconstructability of the AFDM effective channel matrix. Correspondingly, we propose a low-complexity channel estimation scheme, called embedded pilot-aided diagonal reconstruction (EPA-DR), for MIMO-AFDM. Extensive analyses are conducted to demonstrate the influence of fractional Doppler on channel estimation.
- Finally, to show that AFDMA is a promising candidate for next-generation multiple access networks, we propose an orthogonal resource allocation scheme for AFDMA system based on the EPA-DR channel estimation method. By exploring the differences in the delay-Doppler profiles between the base station and all the users, we manage to reduce the guard symbol overhead to the greatest extent.

The rest of this paper is organized as follows. Section II reviews the basic concepts of AFDM and introduces MIMO-AFDM system, which lays the foundations for its diversity analysis in Section III. Section IV presents the channel estimation for MIMO-AFDM, followed by the resource allocation for AFDMA in Section V. Simulation results are presented in Section VI, while Section VII concludes this paper.

Notations: Symbols $\mathbf{a}[i]$ and $\mathbf{A}[i, j]$ denote the i -th element

of \mathbf{a} and the (i, j) -th element of \mathbf{A} respectively; \mathbb{C} denotes the set of complex numbers and $\mathbb{C}^{M \times N}$ denotes the set of all $M \times N$ matrices with complex entries; \mathbf{I}_N denotes the identity matrix of size $N \times N$; $\mathbf{a} \sim \mathcal{CN}(\mathbf{0}, N_0 \mathbf{I}_N)$ means that \mathbf{a} follows the complex Gaussian distribution with zero mean and covariance $N_0 \mathbf{I}_N$; $\delta(\cdot)$ denotes the Dirac delta function; $\text{diag}(\cdot)$ denotes a square diagonal matrix with the elements of input vector on the main diagonal; $(\cdot)^H$, $(\cdot)^T$ and $\|\cdot\|$ denote the transpose, the Hermitian and the Euclidean norm operations; $|\cdot|$ denotes the absolute value of a complex scalar; $(\cdot)_N$ denotes the modulus operation with respect to N ; $\mathbb{E}[\cdot]$ denotes the expectation; $Q(\cdot)$ denotes the tail distribution function of the standard normal distribution.

II. AFDM SYSTEM

In this section, the basic concepts of AFDM from [21] and [22] are reviewed. Based on that, we establish the settings of MIMO-AFDM system.

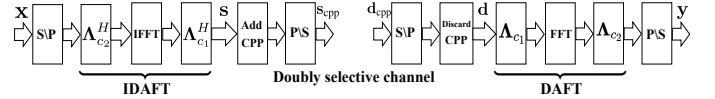


Fig. 1. SISO-AFDM modulation/demodulation block diagrams.

A. SISO-AFDM System

1) Channel model: Assume the doubly selective channel has the following impulse response at time n and delay l

$$g_n(l) = \sum_{i=1}^P h_i e^{-j \frac{2\pi}{N} \nu_i n} \delta(l - l_i) \quad (1)$$

where P is the number of propagation paths, h_i is the channel gain of the i -th path, $l_i \in [0, l_{\max}]$ is the associated delay normalized with sample period and is assumed to be a non-negative integer¹, l_{\max} denotes the maximum delay. While $\nu_i = \alpha_i + \beta_i$ represents the associated Doppler normalized with subcarrier spacing and has a finite support bounded by $[-\nu_{\max}, \nu_{\max}]$, where $\alpha_i \in [-\alpha_{\max}, \alpha_{\max}]$ and $\beta_i \in (-\frac{1}{2}, \frac{1}{2}]$ are the integer and fractional part of ν_i respectively, ν_{\max} denotes the maximum Doppler and α_{\max} denotes the integer part of ν_{\max} . In this paper, we assume that P is unknown while l_{\max} and ν_{\max} are known in advance [32].

2) AFDM modulation: Fig. 1 shows the modulation/demodulation block diagrams of SISO-AFDM system. Let $\mathbf{x} \in \mathbb{A}^{N \times 1}$ denotes a vector of N quadrature amplitude modulation (QAM) symbols that reside on the DAFT domain, where N denotes the number of subcarriers, \mathbb{A} represents the modulation alphabet. After the serial to parallel operation, N points inverse DAFT (IDAFT) is performed to map \mathbf{x} to the time domain as

$$s[n] = \frac{1}{\sqrt{N}} \sum_{m=0}^{N-1} x[m] e^{j2\pi(c_2 m^2 + \frac{1}{N} mn + c_1 n^2)} \quad (2)$$

¹Fractional delays can be ignored in typical wide-band systems [14]. The extension to fractional delays in narrow-band systems will be considered in our future work.

where $m = 0, \dots, N-1$ denotes the index of subcarriers, c_1 and c_2 are two AFDM parameters. Equation (2) can be written in matrix form as

$$\mathbf{s} = \mathbf{\Lambda}_{c_1}^H \mathbf{F}^H \mathbf{\Lambda}_{c_2}^H \mathbf{x} = \mathbf{A}^H \mathbf{x} \quad (3)$$

where $\mathbf{A} = \mathbf{\Lambda}_{c_2} \mathbf{F} \mathbf{\Lambda}_{c_1} \in \mathbb{C}^{N \times N}$ represents the DAFT matrix, $\mathbf{\Lambda}_c = \text{diag}(e^{-j2\pi c n^2}, n = 0, 1, \dots, N-1)$. \mathbf{F} is the DFT matrix with entries $e^{-j2\pi mn/N} / \sqrt{N}$. Before transmitting \mathbf{s} , an N_{cpp} -long *chirp-periodic* prefix (CPP) should be added, which plays the same role as the cyclic prefix (CP) in OFDM to cope with the multipath propagation, and makes the channel lie in a periodic domain equivalently, N_{cpp} is any integer no less than the l_{max} of the wireless channel. The prefix can be expressed as

$$s[n] = s[N+n]e^{-j2\pi c_1(N^2+2Nn)}, \quad n = -N_{\text{cpp}}, \dots, -1. \quad (4)$$

We can notice that CPP equals to CP whenever $2Nc_1$ is an integer and N is even.

3) AFDM demodulation: At the receiver, the received time domain symbols \mathbf{d}_{cpp} can be expressed as

$$\mathbf{d}_{\text{cpp}}[n] = \sum_{l=0}^{\infty} s_{\text{cpp}}[n-l]g_n(l) + v[n] \quad (5)$$

where $v \sim \mathcal{CN}(0, N_0)$ represents the noise in time domain. After the serial to parallel operation and discarding CPP, the relationship between the CPP-free time domain symbols at the transmitter and receiver can be vectorized as

$$\mathbf{d} = \sum_{i=1}^P h_i \tilde{\mathbf{H}}_i \mathbf{s} + \mathbf{v} = \tilde{\mathbf{H}} \mathbf{s} + \mathbf{v} \quad (6)$$

where $\mathbf{v} \sim \mathcal{CN}(\mathbf{0}, N_0 \mathbf{I}_N)$ is the time domain noise vector, $\tilde{\mathbf{H}} \in \mathbb{C}^{N \times N}$ denotes the effective time domain channel matrix, $\tilde{\mathbf{H}}_i = \mathbf{\Gamma}_{\text{CPP}_i} \mathbf{\Delta}_{\nu_i} \mathbf{\Pi}^{l_i}$ represents the time domain subchannel matrix of the i -th path (each path can be viewed as one subchannel), $\mathbf{\Pi}$ denotes the forward cyclic-shift matrix which models the delay, while the digital frequency shift matrix $\mathbf{\Delta}_{\nu_i} \triangleq \text{diag}(e^{-j\frac{2\pi}{N}\nu_i n}, n = 0, 1, \dots, N-1)$ models the Doppler. The effective CPP matrix $\mathbf{\Gamma}_{\text{CPP}_i}$ with a size of $N \times N$ is given by

$$\mathbf{\Gamma}_{\text{CPP}_i} = \text{diag} \left(\begin{cases} e^{-j2\pi c_1(N^2-2N(l_i-n))} & n < l_i \\ 1 & n \geq l_i \end{cases} \right). \quad (7)$$

Finally, N point DAFT is implemented and the received time domain symbols \mathbf{d} are transformed to the DAFT domain symbols \mathbf{y} with

$$y[m] = \frac{1}{\sqrt{N}} \sum_{n=0}^{N-1} d[n] e^{-j2\pi(c_2 m^2 + \frac{1}{N} mn + c_2 n^2)} + w[m] \quad (8)$$

where w represents the noise in the DAFT domain. The matrix representation of (8) is

$$\mathbf{y} = \mathbf{\Lambda}_{c_2} \mathbf{F} \mathbf{\Lambda}_{c_1} \mathbf{d} = \mathbf{A} \mathbf{d}. \quad (9)$$

Since \mathbf{A} is a unitary matrix, w has the same statistical properties as v .

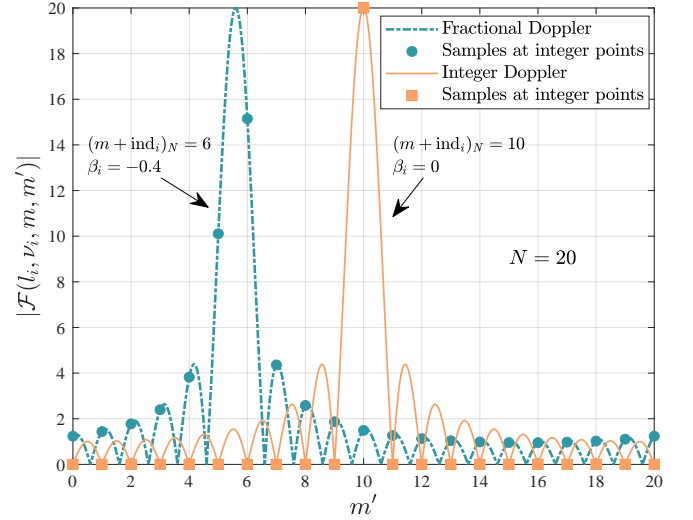


Fig. 2. The value of $|\mathcal{F}(l_i, \nu_i, m, m')|$ in the cases of fractional Doppler and integer Doppler.

4) Input-output relationship: Substituting (1), (2) and (5) into (8), we have the input-output relationship of SISO-AFDM system [21] in the DAFT domain as shown in (10) on the next page, where the index indicator $\text{ind}_i \triangleq (\alpha_i + 2Nc_1 l_i)_N$, and

$$\mathcal{C}(l_i, m, m') = e^{j\frac{2\pi}{N}(Nc_1 l_i^2 - m' l_i + Nc_2(m'^2 - m^2))} \quad (11)$$

is a complex exponential with energy of one. The spreading factor is given by

$$\mathcal{F}(l_i, \nu_i, m, m') = \frac{e^{j2\pi(m + \text{ind}_i - m' + \beta_i)} - 1}{e^{j\frac{2\pi}{N}(m + \text{ind}_i - m' + \beta_i)} - 1}. \quad (12)$$

As shown in Fig. 2, its magnitude $|\mathcal{F}(l_i, \nu_i, m, m')|$ reaches the peak at $m' = (m + \text{ind}_i)_N$ and decreases as m' moves away from $(m + \text{ind}_i)_N$. For the convenience of illustration, we define $\mathcal{E}(l_i, \nu_i, m, m')$ in (10) as

$$\mathcal{E}(l_i, \nu_i, m, m') \triangleq \frac{1}{N} \mathcal{C}(l_i, m, m') \mathcal{F}(l_i, \nu_i, m, m'). \quad (13)$$

The matrix form of (10) can be obtained by substituting (3) and (6) into (9) as

$$\mathbf{y} = \sum_{i=1}^P h_i \mathbf{H}_i \mathbf{x} + \mathbf{w} = \mathbf{H}_{\text{eff}} \mathbf{x} + \mathbf{w} \quad (14)$$

where $\mathbf{H}_i = \mathbf{A} \tilde{\mathbf{H}}_i \mathbf{A}^H$ denotes the DAFT domain subchannel matrix of the i -th path, $\mathbf{H}_{\text{eff}} = \mathbf{A} \tilde{\mathbf{H}} \mathbf{A}^H \in \mathbb{C}^{N \times N}$ is the effective channel matrix, $\mathbf{w} \sim \mathcal{CN}(\mathbf{0}, N_0 \mathbf{I}_N)$ is the DAFT domain noise vector. Note that

$$\mathbf{H}_i[m, m'] = \mathcal{E}(l_i, \nu_i, m, m') \quad (15)$$

and

$$\mathbf{H}_{\text{eff}}[m, m'] = \sum_{i=1}^P h_i \mathbf{H}_i[m, m'] = \sum_{i=1}^P h_i \mathcal{E}(l_i, \nu_i, m, m') \quad (16)$$

with $m, m' \in [0, N-1]$. As proven in [21] (Theorem 1), as long as $c_1 \geq \frac{2(\alpha_{\text{max}} + k_\nu) + 1}{2N}$, where k_ν is a non-negative integer used to combat the fractional Doppler and will be illustrated

$$\begin{aligned}
y[m] &= \frac{1}{N} \sum_{m'=0}^{N-1} \sum_{i=1}^P h_i \underbrace{e^{j\frac{2\pi}{N}(Nc_1l_i^2 - m'l_i + Nc_2(m'^2 - m^2))}}_{\mathcal{C}(l_i, m, m')} \underbrace{\frac{e^{j2\pi(m + \text{ind}_i - m' + \beta_i)} - 1}{e^{j\frac{2\pi}{N}(m + \text{ind}_i - m' + \beta_i)} - 1}}_{\text{Spreading factor } \mathcal{F}(l_i, \nu_i, m, m')} x[m'] + w[m] \\
&= \sum_{m'=0}^{N-1} \sum_{i=1}^P h_i \mathcal{E}(l_i, \nu_i, m, m') x[m'] + w[m], \quad 0 \leq m \leq N-1
\end{aligned} \tag{10}$$

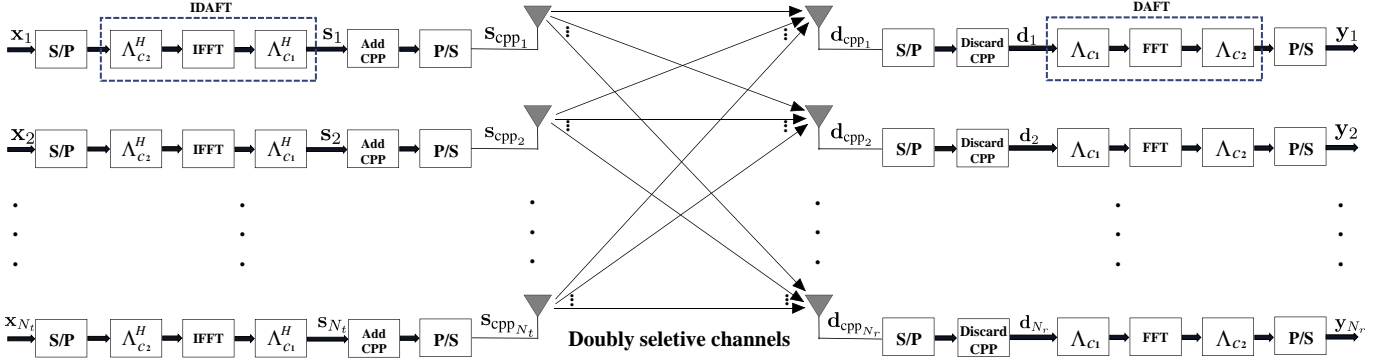


Fig. 3. $N_t \times N_r$ MIMO-AFDM modulation/demodulation block diagrams.

in Section IV-B, and c_2 is either an arbitrary irrational number or a rational number sufficiently smaller than $\frac{1}{2N}$, AFDM can achieve full diversity in doubly selective channels.

B. MIMO-AFDM System

We next introduce MIMO-AFDM system with its modulation/demodulation block diagrams provided in Fig. 3. Let N_t and N_r denote the number of transmit antennas (TA) and receive antennas (RA) respectively. Then the linear system model based input-output relationship between the r -th RA and N_t TAs from an $N_t \times N_r$ MIMO-AFDM system can be derived from (10) as

$$y_r[m] = \sum_{t=1}^{N_t} \sum_{m'=0}^{N-1} \sum_{i=1}^P h_i^{[r,t]} \mathcal{E}(l_i, \nu_i, m, m') x_t[m'] + w_r[m] \tag{17}$$

where $m \in [0, N-1]$, integer $r \in [1, N_r]$ and $t \in [1, N_t]$ denote the index of the RA and TA respectively, $h_i^{[r,t]}$ is the channel gain of the i -th path between the r -th RA and the t -th TA, $w_r \sim \mathcal{CN}(0, N_0)$ represents the noise in DATF domain at the r -th RA. Then the matrix form of the input-output relationships between all pairs of RAs and TAs can be denoted as

$$\mathbf{y}_1 = \mathbf{H}_{1,1}\mathbf{x}_1 + \mathbf{H}_{1,2}\mathbf{x}_2 + \cdots + \mathbf{H}_{1,N_t}\mathbf{x}_{N_t} + \mathbf{w}_1$$

$$\mathbf{y}_2 = \mathbf{H}_{2,1}\mathbf{x}_1 + \mathbf{H}_{2,2}\mathbf{x}_2 + \cdots + \mathbf{H}_{2,N_t}\mathbf{x}_{N_t} + \mathbf{w}_2$$

\vdots

$$\mathbf{y}_{N_r} = \mathbf{H}_{N_r,1}\mathbf{x}_1 + \mathbf{H}_{N_r,2}\mathbf{x}_2 + \cdots + \mathbf{H}_{N_r,N_t}\mathbf{x}_{N_t} + \mathbf{w}_{N_r} \tag{18}$$

with $\mathbf{H}_{r,t} = \mathbf{A}\tilde{\mathbf{H}}_{r,t}\mathbf{A}^H$ representing the effective channel matrix between the r -th RA and the t -th TA, $\tilde{\mathbf{H}}_{r,t}$ being the associated time domain channel matrix, noise vector $\mathbf{w} \sim \mathcal{CN}(\mathbf{0}, N_0\mathbf{I}_N)$. For the sake of compactedness, we define the

effective MIMO channel matrix for the above MIMO-AFDM system as

$$\mathbf{H}_{\text{MIMO}} = \begin{bmatrix} \mathbf{H}_{1,1} & \mathbf{H}_{1,2} & \cdots & \mathbf{H}_{1,N_t} \\ \mathbf{H}_{2,1} & \mathbf{H}_{2,2} & \cdots & \mathbf{H}_{2,N_t} \\ \vdots & \vdots & \ddots & \vdots \\ \mathbf{H}_{N_r,1} & \mathbf{H}_{N_r,2} & \cdots & \mathbf{H}_{N_r,N_t} \end{bmatrix} \tag{19}$$

where $\mathbf{H}_{\text{MIMO}} \in \mathbb{C}^{N N_r \times N N_t}$, transmitted vector $\mathbf{x}_{\text{MIMO}} = [\mathbf{x}_1^T, \mathbf{x}_2^T, \cdots, \mathbf{x}_{N_t}^T]^T \in \mathbb{C}^{N N_t \times 1}$, received vector $\mathbf{y}_{\text{MIMO}} = [\mathbf{y}_1^T, \mathbf{y}_2^T, \cdots, \mathbf{y}_{N_r}^T]^T \in \mathbb{C}^{N N_r \times 1}$, and noise vector $\mathbf{w}_{\text{MIMO}} = [\mathbf{w}_1^T, \mathbf{w}_2^T, \cdots, \mathbf{w}_{N_r}^T]^T \in \mathbb{C}^{N N_r \times 1}$. Then (18) can be rewritten as

$$\mathbf{y}_{\text{MIMO}} = \mathbf{H}_{\text{MIMO}}\mathbf{x}_{\text{MIMO}} + \mathbf{w}_{\text{MIMO}}. \tag{20}$$

Many low-complexity detectors proposed for AFDM and OTFS can be applied to the signal detection of MIMO-AFDM directly [28], [33]–[35]. We adopt the widely-used message passing (MP) detector proposed in [33] to evaluate the performance of MIMO-AFDM in large frame sizes. In the sequel, we study the performance of MIMO-AFDM with perfect and imperfect CSI.

III. DIVERSITY ANALYSIS OF MIMO-AFDM

In this section, we derive the diversity order of MIMO-AFDM. For ease of derivations, we assume the delay and Doppler shifts as integers. Simulation results given in Section VI-A show that the derived diversity order for integer Doppler also holds for the fractional Doppler case.

Considering there are P propagation paths between all pairs of RAs and TAs, and the fractional parts of all the associated

Doppler shifts are zero ($\beta_i s = 0$ and $k_\nu = 0$), then the spreading factor $\mathcal{F}(l_i, \nu_i, m, m')$ in (12) satisfies

$$\mathcal{F}(l_i, \nu_i, m, m') = \frac{e^{j2\pi(m+\text{ind}_i-m')-1}}{e^{j\frac{2\pi}{N}(m+\text{ind}_i-m')}-1} = \begin{cases} N, & m' = (m + \text{ind}_i)_N \\ 0, & \text{otherwise.} \end{cases} \quad (21)$$

Hence, we have

$$\mathcal{E}(l_i, \nu_i, m, m') = \begin{cases} \mathcal{C}(l_i, m, m'), & m' = (m + \text{ind}_i)_N \\ 0, & m' \neq (m + \text{ind}_i)_N. \end{cases} \quad (22)$$

Then the input-output relationship of SISO-AFDM in (10) can be simplified as

$$y[m] = \sum_{i=1}^P h_i \mathcal{C}(l_i, m, m') x[m'] + w[m] \quad (23)$$

where $m \in [0, N-1]$, $m' = (m + \text{ind}_i)_N$. Therefore, there are P non-zero elements in each row and column of $\mathbf{H}_{r,t}$, $\forall r \in [1, N_r], t \in [1, N_t]$. Equation (14) can then be presented in an alternate way as [21]

$$\mathbf{y} = \sum_{i=1}^P h_i \mathbf{H}_i \mathbf{x} + \mathbf{w} = \tilde{\Phi}(\mathbf{x}) \mathbf{h} + \mathbf{w} \quad (24)$$

where $\tilde{\Phi}(\mathbf{x}) = [\mathbf{H}_1 \mathbf{x}, \mathbf{H}_2 \mathbf{x}, \dots, \mathbf{H}_P \mathbf{x}] \in \mathbb{C}^{N \times P}$, channel gain vector $\mathbf{h} = [h_1, h_2, \dots, h_P]^T \in \mathbb{C}^{P \times 1}$.

Similarly, the input-output relationship of MIMO-AFDM in (17) can be simplified as

$$y_r[m] = \sum_{t=1}^{N_t} \sum_{i=1}^P h_i^{[r,t]} \mathcal{C}(l_i, m, m') x_t[m'] + w_r[m] \quad (25)$$

where $m \in [0, N-1]$, $m' = (m + \text{ind}_i)_N$. From (25) we can see that each row of \mathbf{H}_{MIMO} has only $P N_t$ non-zero elements. Therefore, the vectorized input-output relationship in (20) can also be presented as

$$\mathbf{Y} = \tilde{\Phi}(\mathbf{X}) \tilde{\mathbf{h}} + \mathbf{W} \quad (26)$$

where received symbol matrix $\mathbf{Y} = [\mathbf{y}_1, \mathbf{y}_2, \dots, \mathbf{y}_{N_r}]$ is an $N \times N_r$ matrix whose r -th column is the received symbol vector of the r -th RA, transmitted symbol matrix $\mathbf{X} = [\mathbf{x}_1, \mathbf{x}_2, \dots, \mathbf{x}_{N_t}]$ is an $N \times N_t$ matrix whose t -th column is the transmitted symbol vector of the t -th TA, $\tilde{\Phi}(\mathbf{X})$ is an $N \times P N_t$ concatenated matrix with a definition of

$$\tilde{\Phi}(\mathbf{X}) = [\Phi(\mathbf{x}_1), \Phi(\mathbf{x}_2), \dots, \Phi(\mathbf{x}_{N_t})] \quad (27)$$

$\tilde{\mathbf{h}} \in \mathbb{C}^{P N_t \times N_r}$ is channel gain matrix with a definition of

$$\tilde{\mathbf{h}} = \begin{bmatrix} \mathbf{h}_{1,1} & \mathbf{h}_{2,1} & \dots & \mathbf{h}_{N_r,1} \\ \mathbf{h}_{1,2} & \mathbf{h}_{2,2} & \dots & \mathbf{h}_{N_r,2} \\ \vdots & \vdots & \ddots & \vdots \\ \mathbf{h}_{1,N_t} & \mathbf{h}_{2,N_t} & \dots & \mathbf{h}_{N_r,N_t} \end{bmatrix} \quad (28)$$

where $\mathbf{h}_{r,t} \in \mathbb{C}^{P \times 1}$ denotes the channel gain vector between the r -th RA and t -th TA, and its elements $h_i^{r,t}$ are assumed to follow the distribution of $\mathcal{CN}(0, 1/P)$ (uniform scattering profile), $\mathbf{W} \in \mathbb{C}^{N \times N_r}$ is the noise matrix.

For convenience, we normalize the transmit symbol matrix \mathbf{X} so that the signal-to-noise ratio (SNR) at each receive antenna is $\frac{1}{N_o}$. Let \mathbf{X}_i and \mathbf{X}_j be two transmit symbol matrices. Assuming perfect CSI and maximum likelihood (ML) detection at the receiver, the probability of transmitting the symbol matrix \mathbf{X}_i and deciding in favor of \mathbf{X}_j at the receiver is the pairwise error probability (PEP) between \mathbf{X}_i and \mathbf{X}_j , which can be expressed as [36]

$$P(\mathbf{X}_i \rightarrow \mathbf{X}_j | \tilde{\mathbf{h}}, \mathbf{X}_i) = Q \left(\sqrt{\frac{\|(\tilde{\Phi}(\mathbf{X}_i) - \tilde{\Phi}(\mathbf{X}_j)) \tilde{\mathbf{h}}\|^2}{2N_o}} \right). \quad (29)$$

The PEP averaged over the channel statistics can be denoted as

$$P(\mathbf{X}_i \rightarrow \mathbf{X}_j) = \mathbb{E} \left[Q \left(\sqrt{\frac{\|(\tilde{\Phi}(\mathbf{X}_i) - \tilde{\Phi}(\mathbf{X}_j)) \tilde{\mathbf{h}}\|^2}{2N_o}} \right) \right]. \quad (30)$$

Define difference matrix as $\delta^{(i,j)} \triangleq \mathbf{X}_i - \mathbf{X}_j$, where the t -th column of $\delta^{(i,j)}$ is $\delta_t^{(i,j)} = \mathbf{x}_t^{(i)} - \mathbf{x}_t^{(j)}$, which denotes the difference of two transmitted symbols at the t -th TA. Since $\tilde{\Phi}$ is a linear operator, we have

$$P(\mathbf{X}_i \rightarrow \mathbf{X}_j) = \mathbb{E} \left[Q \left(\sqrt{\frac{\|\tilde{\Phi}(\delta^{(i,j)}) \tilde{\mathbf{h}}\|^2}{2N_o}} \right) \right]. \quad (31)$$

Using Chernoff bound and the fact that each TA transmits independent AFDM symbols, an upper bound on the PEP in (31) can be obtained as [36]

$$P(\mathbf{X}_i \rightarrow \mathbf{X}_j) \leq \left(\prod_{l=1}^k \frac{1}{1 + \frac{\lambda_{t,l}^2}{4PN_o}} \right)^{N_r} \quad (32)$$

where $\lambda_{t,l}$ is the l -th singular value of the matrix $\tilde{\Phi}(\delta_t^{(i,j)})$ ($t \in 1, 2, \dots, N_t$) and k is the rank of $\tilde{\Phi}(\delta_t^{(i,j)})$. At high SNR regime, (32) can be further simplified as

$$P(\mathbf{X}_i \rightarrow \mathbf{X}_j) \leq \frac{1}{N_o^{kN_r}} \left(\prod_{l=1}^k \frac{\lambda_{t,l}^2}{4P} \right)^{-N_r}. \quad (33)$$

We can observe from (33) that the exponent of the SNR term $\frac{1}{N_o}$ is kN_r , and the overall bit error ratio (BER) is dominated by the PEP with the minimum value of k , for all $i, j, i \neq j$. Therefore, the diversity order of MIMO-AFDM, denoted by ρ , is given by

$$\rho = N_r \cdot \min_{i,j,i \neq j} \text{rank}(\tilde{\Phi}(\delta_t^{(i,j)})). \quad (34)$$

In [21] (APPENDIX A), the term $\min_{i,j,i \neq j} \text{rank}(\tilde{\Phi}(\delta_t^{(i,j)}))$ is proven to be P whenever the AFDM parameters c_1 and c_2 are tuned as described at the end of Section II-A, and the number of subcarriers N satisfies

$$N \geq (l_{\max} + 1)(2\alpha_{\max} + 1). \quad (35)$$

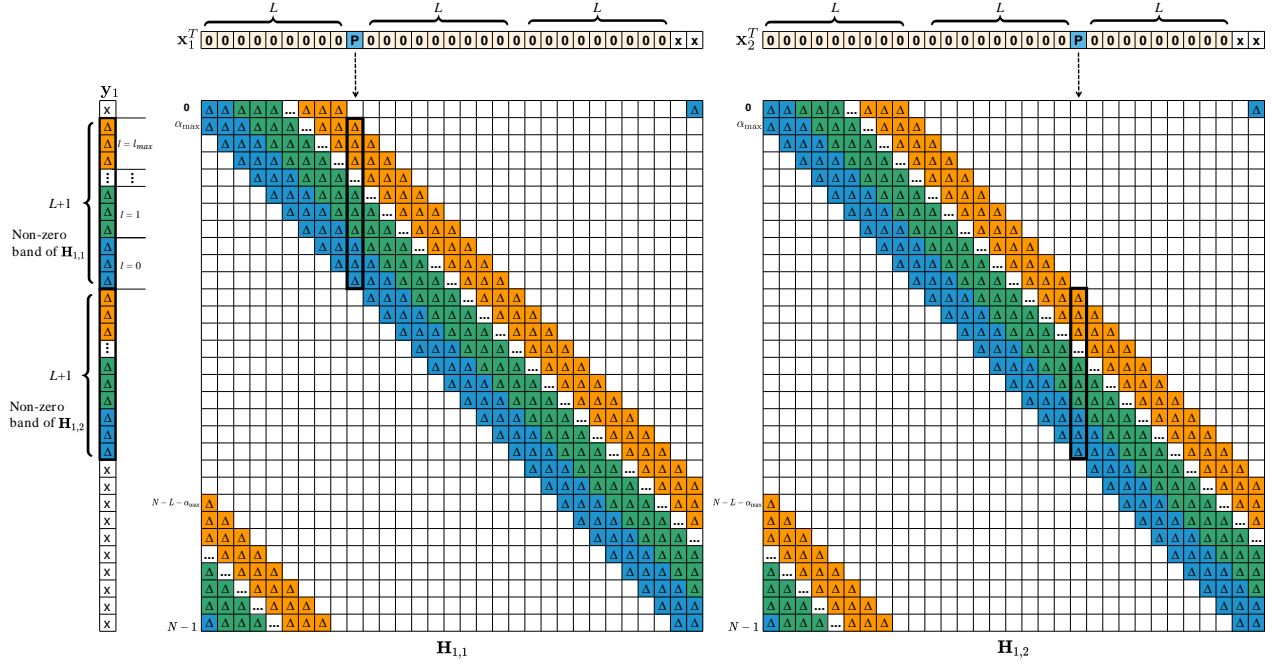


Fig. 4. EPA-DR for 2×1 MISO-AFDM system with integer Doppler ('P':pilot, '0':guard, 'x':data, ' Δ ': possible non-zero value, 'blank' in $\mathbf{H}_{r,t}$: 0).

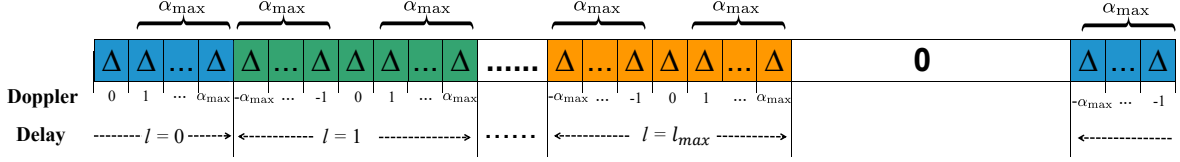


Fig. 5. The bijective relationship between the propagation paths and the non-zero entries in the 0-th row or the $(N-1)$ -th column of $\mathbf{H}_{r,t}$ with integer Doppler (' Δ ': possible non-zero value).

In practice, $N \gg (l_{\max} + 1)(2\alpha_{\max} + 1)$, thus the diversity order of MIMO-AFDM is PN_r , i.e., MIMO-AFDM achieves full diversity in doubly selective channels.

IV. CHANNEL ESTIMATION FOR MIMO-AFDM SYSTEM

In practice, \mathbf{H}_{MIMO} must be estimated at the receiver to perform signal detection. To meet this requirement, we propose a low-complexity channel estimation scheme for MIMO-AFDM system based on the diagonal reconstructability of the AFDM effective channel matrix.

A. Integer Doppler Case

1) Effective channel matrix analysis: Consider $\beta_i s = 0$, $k_\nu = 0$ and $c_1 = \frac{2\alpha_{\max}+1}{2N}$. Define $L \triangleq (l_{\max} + 1)(2\alpha_{\max} + 1) - 1$, where $L + 1 \ll N$ (i.e., the channels are underspread), then there are at most $L + 1$ propagation paths exist in the channel. From (15) and (22), we have

$$\mathbf{H}_i[m, m'] = \begin{cases} \mathcal{C}(l_i, m, m'), & m' = (m + \text{ind}_i)_N, \\ 0, & m' \neq (m + \text{ind}_i)_N \end{cases} \quad (36)$$

with $m, m' \in [0, N - 1]$, which means there is only one non-zero entry in each row and each column of \mathbf{H}_i . The index of the non-zero entry in the m -th row of \mathbf{H}_i is $(m + \text{ind}_i)_N$, $\text{ind}_i \triangleq (\alpha_i + 2Nc_1l_i)_N = (\alpha_i + (2\alpha_{\max} + 1)l_i)_N$, showing

that it is determined by the delay-Doppler profile (l_i, α_i) of the i -th path and AFDM parameter c_1 jointly, and the non-zero entries is "diagonally" distributed in \mathbf{H}_i . Since $c_1 = \frac{2\alpha_{\max}+1}{2N}$, the non-zero entry coordinates among different \mathbf{H}_i s do not coincide with each other [22].

Substituting (36) into (16), we have

$$\mathbf{H}_{\text{eff}}[m, m'] = \begin{cases} h_i \mathcal{C}(l_i, m, m'), & m' = (m + \text{ind}_i)_N \\ & i = 1, \dots, P \\ 0, & \text{otherwise} \end{cases} \quad (37)$$

where $m, m' \in [0, N - 1]$. Consequently, there is a possible non-zero band with a size of $L + 1$ in each row and each column of \mathbf{H}_{eff} representing $L + 1$ possible paths, as an example $\mathbf{H}_{1,1}$ shown in Fig. 4 (since we assume the channel has P paths, there are only P actual non-zero entries in each band). We can observe that \mathbf{H}_{eff} possesses a cyclic diagonal and sparse structure [21]. The bijective relationship between the delay-Doppler profiles of paths and the non-zero entries from an arbitrary row or column of \mathbf{H}_{eff} is illustrated in Fig. 5. Once the AFDM parameter c_1 is determined, the bijective relationship is determined. For the convenience of illustration, we divide the possible non-zero entry band into $l_{\max} + 1$ delay blocks with different colors.

Moreover, based on the definition of $\mathcal{C}(l_i, m, m')$ in (10),

we can define a transform factor $\mathcal{T}(l_i, m, m')$ as

$$\begin{aligned} \mathcal{T}(l_i, m, m') &= \frac{\mathcal{C}(l_i, (m+1)_N, (m'+1)_N)}{\mathcal{C}(l_i, m, m')} \\ &= e^{j\frac{2\pi}{N}((m'-(m'+1)_N)l_i + Nc_2[(m'+1)_N^2 + m^2 - ((m+1)_N)^2 - m'^2])} \\ &= \begin{cases} e^{j\frac{2\pi}{N}(-l_i + 2Nc_2(m'-m))}, & m < N-1, m' < N-1 \\ e^{j\frac{2\pi}{N}(-l_i + Nc_2(m^2 + 2m' + 1))}, & m = N-1, m' < N-1 \\ e^{j\frac{2\pi}{N}(-l_i - Nc_2(m'^2 + 2m + 1))}, & m < N-1, m' = N-1 \\ e^{-j\frac{2\pi}{N}l_i}, & m = N-1, m' = N-1 \end{cases} \end{aligned} \quad (38)$$

with $m, m' \in [0, N-1]$. It is important to notice that $\mathcal{T}(l_i, m, m')$ has no relevance to the Doppler shift ν_i .

Consequently, according to (37), as long as $\mathbf{H}_{\text{eff}}[m, m']$ is obtained, where (m, m') is a coordinate corresponding to the l -th delay block, $\mathbf{H}_{\text{eff}}[(m+1)_N, (m'+1)_N]$ can be calculated directly using (38) as

$$\mathbf{H}_{\text{eff}}[(m+1)_N, (m'+1)_N] = \mathcal{T}(l, m, m')\mathbf{H}_{\text{eff}}[m, m']. \quad (39)$$

Hence, the non-zeros band of all the columns in \mathbf{H}_{eff} can be reconstructed diagonally as long as one of them is acquired. We refer to this unique characteristic of \mathbf{H}_{eff} as diagonal reconstructability.

2) Channel estimation scheme: Based on the above analysis, we arrange the pilot, guard and data symbols in the DAFT domain at the t -th TA ($t = 1, \dots, N_t$) as

$$x_t[m] = \begin{cases} x_t^{\text{pilot}}, & m = (L+1)t - 1 \\ 0, & m \in [0, (L+1)N_t + L - 1] \\ & \text{and } m \neq (L+1)t - 1 \\ x_t^{\text{data}}[m], & m \in [m_d, N-1] \end{cases} \quad (40)$$

where x_t^{pilot} is the pilot at of t -th TA, the index of pilot at the t -th TA is $m_t^{\text{pilot}} = (L+1)t - 1$, $x_t^{\text{data}}[m]$ is the data symbol in the m -th slot of the t -th TA, $m_d = (L+1)N_t + L$ represents the index of the first data symbol. An example of 2×1 MISO-AFDM system is presented in Fig. 4.

The main idea of the symbol arrangement in (40) is embedding one pilot in the transmitted AFDM symbol at each TA to extract a non-zero band from $\mathbf{H}_{r,t}$. Zero guard symbols must be placed in the adjacency of the pilot. The pilot and guard overhead for each transmit antenna in an $N_t \times N_r$ MIMO-AFDM system is given by

$$O_{\text{CE}} = (N_t + 1)L + N_t \quad (41)$$

where 'CE' stands for channel estimation.

At the r -th RA ($r = 1, \dots, N_r$), the indices of received symbols $y_r[m]$ s that are used for the channel estimation between the r -th RA and the t -th TA are

$$m \in [\alpha_{\max} + (L+1)(t-1), \alpha_{\max} + (L+1)t - 1]. \quad (42)$$

According to (18), these received symbols are just the noise containing non-zero band in the m_t^{pilot} -th column of $\mathbf{H}_{r,t}$ (multiplied by x_t^{pilot}). Then threshold-based energy detection is performed to combat the interference from the noise w_r in (17), i.e.,

$$\hat{\mathbf{H}}_{r,t}[m, m_t^{\text{pilot}}] = \begin{cases} \frac{y_r[m]}{x_t^{\text{pilot}}}, & |y_r[m]| \geq \zeta \\ 0, & \text{otherwise.} \end{cases} \quad (43)$$

By adjusting the threshold ζ , we can alter the miss detection or false alarm probabilities on energy detection, as shown in simulation results in Section VI-B.

Different from the EPA-AML channel estimation scheme proposed in [21], which first estimate the channel parameters (channel gains, delay and Doppler shifts of all the paths) and then reconstruct $\mathbf{H}_{r,t}$, we use (39) to reconstruct $\mathbf{H}_{r,t}$ directly. We name the above procedures used to estimate $\mathbf{H}_{r,t}$ as embedded pilot-aided diagonal reconstruction (EPA-DR) scheme and summarize it in Algorithm 1. The total computation complexity of the EPA-DR scheme is dominated by **Step 3** at the receiver, which requires at most only $(L+1)(N-1)$ complex multiplications² (assume the energy of all the received pilot symbols exceeds the threshold).

Algorithm 1: EPA-DR scheme for \mathbf{H}_{MIMO} estimation

-Transmitter

Input: $l_{\max}, \alpha_{\max}, c_1, c_2, N_t$ and $m_t^{\text{pilot}}, t = 1, \dots, N_t$.

for $t = 1, 2, \dots, N_t$ **do**

 Arrange the pilot, guard, and data symbols at the t -th transmit antenna according to (40).

end

-Receiver

Input: $l_{\max}, \alpha_{\max}, c_1, c_2, \zeta, N_t, N_r, \zeta, m_t^{\text{pilot}}, t = 1, \dots, N_t$.

1 for $r = 1, 2, \dots, N_r$ **do**

2 for $t = 1, 2, \dots, N_t$ **do**

3 Step 1: Obtain the non-zero band in the m_t^{pilot} -th column of $\mathbf{H}_{r,t}$ from \mathbf{y}_r using (42);

4 Step 2: Perform threshold-based energy detection using (43);

5 Step 3: Reconstruct $\hat{\mathbf{H}}_{r,t}$ using (39).

6 end

7 end

Output: Assemble $\hat{\mathbf{H}}_{r,t}$ into $\hat{\mathbf{H}}_{\text{MIMO}}$ using (19).

With the above EPA-DR scheme, we can estimate the effective channel matrices between all pairs of receive antennas and transmit antennas at the receiver simultaneously. The estimated $\hat{\mathbf{H}}_{\text{MIMO}}$ are then used to detect the received data symbols $y_r[m]$ s, $m \notin [\alpha_{\max}, \alpha_{\max} + (L+1)N_t - 1]$. Note that in the case of integer Doppler, there is no interference among the received pilot symbols from different TAs, or between the received data symbols and the received pilot symbols at each receive antenna.

B. Fractional Doppler Case

1) Effective channel matrix analysis: Considering $\beta_i s \neq 0$, $k_\nu \neq 0$ and $c_1 = \frac{2(\alpha_{\max} + k_\nu) + 1}{2N}$, equations (21), (22) and (36)

²All the transform factors in (38) can be calculated in advance at the receiver once the AFDM parameters c_1 and c_2 are determined (l_i can be obtained from the bijective relationship between the coordinate (m, m') and the l_i -th delay block). Moreover, when $m < N-1$ and $m' < N-1$, $\mathcal{T}(l_i, m, m')$ is determined by $m - m'$, i.e., only four transform factors required for each received pilot symbol (for $m = m'$, it is one). Therefore, the total number of transform factors needed to be calculated in practice is $4L + 1$, whose computation complexity is ignorable.

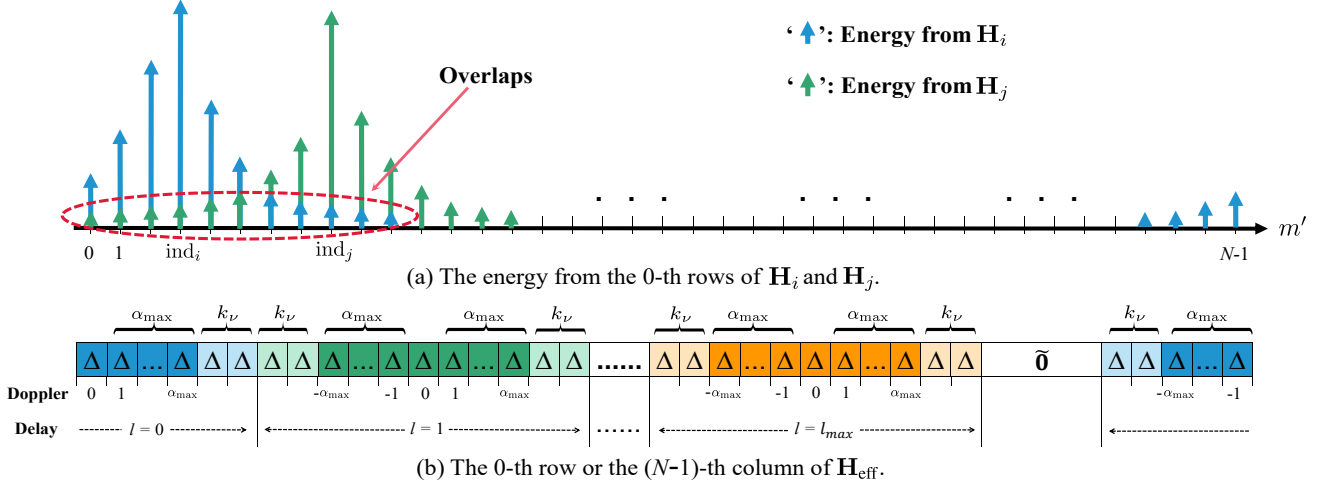


Fig. 6. The influence of fractional Doppler on H_{eff} (Δ : possible large non-zero value, $\tilde{0}$: small value).

no longer hold. Instead, for any subchannel matrix H_i ,

$$H_i[m, m'] = \mathcal{E}(l_i, \nu_i, m, m') \neq 0 \quad (44)$$

with $m, m' \in [0, N-1]$. From (13), we have

$$|\mathcal{E}(l_i, \nu_i, m, m')| = \left| \frac{1}{N} \mathcal{F}(l_i, \nu_i, m, m') \right|. \quad (45)$$

Therefore, in the m -th row of H_i , the index of entry that has the greatest energy is $m' = (m + \text{ind}_i)_N$, where $\text{ind}_i = (\alpha_i + (2(\alpha_{\text{max}} + k_\nu) + 1)l_i)_N$. While the energy of the adjacent entries decays as their indices move away from $(m + \text{ind}_i)_N$, i.e., the smaller the value of $|m + \text{ind}_i - m'|$, the larger energy of $\mathcal{E}(l_i, \nu_i, m, m')$.

For example, the 0-th rows ($m = 0$) of H_i ($l_i = 0, \alpha_i = \alpha_{\text{max}}, \beta_i \neq 0, \text{ind}_i = \alpha_{\text{max}}$) and H_j ($l_j = 1, \alpha_j = -\alpha_{\text{max}}, \beta_j \neq 0, \text{ind}_j = \alpha_{\text{max}} + 2k_\nu + 1$) are provided in Fig. 6(a) to visualize the impact of fractional Doppler. We can see clearly that the fractional Doppler shift ν_i induces non-negligible energy spread from the $(\text{ind}_i)_N$ slot to its adjacency.

The introduction of spacing factor k_ν in c_1 is equivalent to inserting a protection band with a size of k_ν in the head and tail of each delay block. It can alleviate the overlaps between two subchannel matrices with contiguous delay shifts due to the fractional Doppler [21], as the 0-th row or the $(N-1)$ -th column of H_{eff} shown in Fig. 6(b), where $\tilde{0}$ represents small non-zero value. Let $\tilde{L} \triangleq (l_{\text{max}} + 1)(2(\alpha_{\text{max}} + k_\nu) + 1) - 1$, then there is a large value non-zeros band with a size of $\tilde{L} + 1$ in each row and column of H_{eff} , as shown in Fig. 7. Different from the integer Doppler case shown in Fig. 4, the 'blank' slots in H_{eff} with fractional Doppler represent small non-zero values.

For the convenience of illustration, we categorize all the propagation paths according to their delay shifts in the following. We use (l, j) to represent the j -th path with delay l . Then the corresponding Doppler shift, index indicator and channel gain can be denoted as $\nu_{l,j} = \alpha_{l,j} + \beta_{l,j}$, $\text{ind}_{l,j} \triangleq (\alpha_{l,j} + 2Nc_1l)_N$ and $h_{l,j}$, respectively. Denote the number of

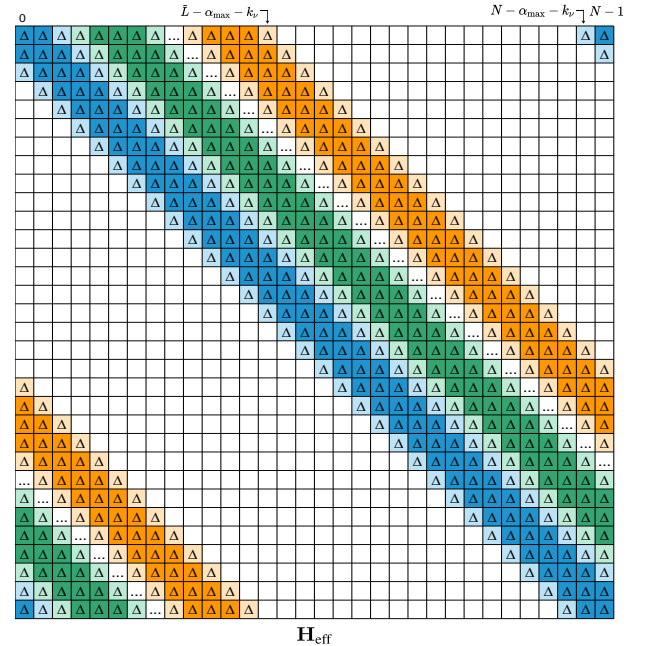


Fig. 7. H_{eff} with fractional Doppler. (Δ : possible large non-zero value, 'blank': small value)

paths with delay l as P_l , where $\sum_{l=0}^{l_{\text{max}}} P_l = P$. Then (16) can be rewritten as

$$H_{\text{eff}}[m, m'] = \sum_{l'=0}^{l_{\text{max}}} \sum_{j=1}^{P_{l'}} h_{l',j} \mathcal{E}(l', \nu_{l',j}, m, m') \quad (46)$$

with $m, m' \in [0, N-1]$.

From (12), we can observe that $\mathcal{F}(l_i, \nu_i, m, m')$ has a period of N with respect to $m - m'$, which means $\mathcal{F}(l_i, \nu_i, (m+1)_N, (m'+1)_N) = \mathcal{F}(l_i, \nu_i, m, m')$. Therefore, for $m \in [0, N-1]$, $m' \in [0, N-1]$, we have

$$\mathcal{E}(l', \nu_{l',j}, (m+1)_N, (m'+1)_N) = \mathcal{T}(l', m, m') \mathcal{E}(l', \nu_{l',j}, m, m'). \quad (47)$$

Hence, it is straightforward that

$$\mathbf{H}_{\text{eff}}[(m+1)_N, (m'+1)_N] = \sum_{l'=0}^{l_{\max}} \mathcal{T}(l', m, m') \sum_{j=1}^{P_{l'}} h_{l',j} \mathcal{E}(l', \nu_{l',j}, m, m'). \quad (48)$$

In particular, when (m, m') is a coordinate that belongs to the l -th delay block in the m' -th column of \mathbf{H}_{eff} , i.e., $\forall j \in [1, P_l]$, $|m + \text{ind}_{l,j} - m'|$ is a small value, whereas $\forall l' \notin l$ and $j \in [1, P_{l'}]$, $|m + \text{ind}_{l',j} - m'|$ is a large value, (46) can be decomposed as

$$\begin{aligned} \mathbf{H}_{\text{eff}}[m, m'] &= \underbrace{\sum_{j=1}^{P_l} h_{l,j} \mathcal{E}(l, \nu_{l,j}, m, m')}_{\bar{\mathbf{H}}_{\text{eff}}[m, m']} \\ &+ \underbrace{\sum_{l'=0, l' \neq l}^{l_{\max}} \sum_{j=1}^{P_{l'}} h_{l',j} \mathcal{E}(l', \nu_{l',j}, m, m')}_{\tilde{\mathbf{H}}_{\text{eff}}[m, m']}. \end{aligned} \quad (49)$$

According to (45), $\bar{\mathbf{H}}_{\text{eff}}[m, m']$ contributes the greatest part to $\mathbf{H}_{\text{eff}}[m, m']$. Hence, we can approximate $\mathbf{H}_{r,t}[m, m']$ as

$$\mathbf{H}_{\text{eff}}[m, m'] \approx \bar{\mathbf{H}}_{\text{eff}}[m, m'] \quad (50)$$

This approximation allows us to obtain an estimation of $\mathbf{H}_{\text{eff}}[(m+1)_N, (m'+1)_N]$, which is given by

$$\begin{aligned} \hat{\mathbf{H}}_{\text{eff}}[(m+1)_N, (m'+1)_N] &= \mathcal{T}(l, m, m') \mathbf{H}_{\text{eff}}[m, m'] \\ &= \mathcal{T}(l, m, m') \underbrace{\sum_{j=1}^{P_l} h_{l,j} \mathcal{E}(l, \nu_{l,j}, m, m')}_{\mathcal{T}(l, m, m') \bar{\mathbf{H}}_{\text{eff}}[m, m']} \\ &+ \underbrace{\mathcal{T}(l, m, m') \sum_{l'=0, l' \neq l}^{l_{\max}} \sum_{j=1}^{P_{l'}} h_{l',j} \mathcal{E}(l', \nu_{l',j}, m, m')}_{\text{IDI}} \end{aligned} \quad (51)$$

where the term $\mathcal{T}(l, m, m') \bar{\mathbf{H}}_{\text{eff}}[m, m'] = \bar{\mathbf{H}}_{\text{eff}}[(m+1)_N, (m'+1)_N]$ is the main component of $\mathbf{H}_{\text{eff}}[(m+1)_N, (m'+1)_N]$, i.e., \mathbf{H}_{eff} retains the diagonal reconstructability approximately in the case of fractional Doppler.

By comparing (48) and (51), we can observe that error is introduced since all the transform factors $\mathcal{T}(l', m, m')$ s in $\mathbf{H}_{\text{eff}}[(m+1)_N, (m'+1)_N]$ corresponding to paths with delay $l' \neq l$ are replaced with $\mathcal{T}(l, m, m')$ in $\hat{\mathbf{H}}_{\text{eff}}[(m+1)_N, (m'+1)_N]$. Naturally, we name this error as inter-delay interference (IDI). By increasing k_ν , the values of $|m + \text{ind}_{l,j} - m'|$ s, $\forall l' \notin l$ and $j \in [1, P_{l'}]$, can be enlarged, making the approximation in (50) more accurate.

2) Channel estimation scheme: We arrange the pilot, guard and data symbols at the t -th TA ($t = 1, \dots, N_t$) similar to the integer Doppler case in (40) as

$$x_t[m] = \begin{cases} x_t^{\text{pilot}}, & m = (\tilde{L} + 1)t - 1 \\ 0, & m \in [0, (\tilde{L} + 1)N_t + \tilde{L} - 1] \\ & \text{and } m \neq (\tilde{L} + 1)t - 1 \\ x_t^{\text{data}}[m], & m \in [\tilde{m}_d, N - 1] \end{cases} \quad (52)$$

where the index of pilot at the t -th TA is $\tilde{m}_t^{\text{pilot}} = (\tilde{L} + 1)t - 1$, the index of the first data symbol is $\tilde{m}_d = (\tilde{L} + 1)N_t + \tilde{L}$. The pilot and guard overhead for each transmit antenna in an $N_t \times N_r$ MIMO-AFDM system is given by

$$\tilde{O}_{\text{CE}} = (N_t + 1)\tilde{L} + N_t. \quad (53)$$

Table I provides the overhead comparison between AFDM and OTFS when conducting embedded pilot-aided channel estimation under different configurations with fractional Doppler (the integer Doppler case can be obtained by setting $k_\nu = 0$). We can see that AFDM maintains its advantage over OTFS on less channel estimation overhead in MIMO system.

At the r -th RA ($r = 1, \dots, N_r$), the indices of received symbols $y_r[m]$ s that are used for the channel estimation between the r -th RA and the t -th TA are

$$m \in [\alpha_{\max} + (\tilde{L} + 1)(t - 1), \alpha_{\max} + (\tilde{L} + 1)t - 1]. \quad (54)$$

Different from the integer Doppler case, these received symbols not only consist of the noise containing large non-zero band from the $\tilde{m}_t^{\text{pilot}}$ -th column of $\mathbf{H}_{r,t}$ (multiplied by x_t^{pilot}), but also some interferences caused by fractional Doppler (since the ‘blank’ slots in the AFDM effective channel matrix represent small non-zero values).

For example, considering $(m, \tilde{m}_t^{\text{pilot}})$ as one of the coordinates that belong to the l -th delay block in the $\tilde{m}_t^{\text{pilot}}$ -th column of $\mathbf{H}_{r,t}$, the received symbol $y_r[m]$ can be decomposed into five components as (55) from (17). According to (49), $\bar{\mathbf{H}}_{r,t}[m, \tilde{m}_t^{\text{pilot}}]x_t^{\text{pilot}}$ contributes the greatest energy to $y_r[m]$. Moreover, due to the fractional Doppler, inter-pilot interference (IPI) and inter-pilot-data interference (IPDI) take place. Since the energy of the pilots is much larger than the data symbols in practice, IPI is more serious than IPDI. After the threshold-based energy detection with (43), we use (51) to reconstruct the whole $\mathbf{H}_{r,t}$ diagonally, where IDI is induced.

In summary, four types of interference are introduced when performing EPA-DR channel estimation with fractional Doppler³. The IPI, IPDI and white gaussian noise are induced in the phase of non-zero bands extraction (**Step 1** in Algorithm 1), while the IDI is induced in the phase of $\mathbf{H}_{r,t}$ s reconstruction (**Step 3** in Algorithm 1). The IPI, IPDI and IDI are all caused by the fractional Doppler and can be suppressed by increasing k_ν . Compared to the EPA-AML channel estimation scheme proposed in [21], which relies on finding the delay and Doppler shifts of the P paths with brute force search and hence suffers from high computation complexity when the value of l_{\max} , α_{\max} or P is large, EPA-DR scheme does not need to know the number of paths in advance and can be applied to some more general scenarios (different paths may have the same delay).

The estimated $\hat{\mathbf{H}}_{\text{MIMO}}$ is then used to detect the receive data symbols $y_r[m]$, $m \notin [\alpha_{\max}, \alpha_{\max} + (\tilde{L} + 1)N_t - 1]$, which is

³The summary of EPA-DR channel estimation scheme in the case of fractional Doppler can be obtained by replacing (40), (42) and (39) with (52), (54) and (51) in Algorithm 1, respectively.

TABLE I
OVERHEAD COMPARISON BETWEEN AFDM AND OTFS APPLYING EMBEDDED PILOT-AIDED
CHANNEL ESTIMATION UNDER DIFFERENT SCENARIOS

Scenario	AFDM	OTFS [14]
SISO - fractional Doppler	$2(l_{\max} + 1)(2(\alpha_{\max} + k_{\nu}) + 1) - 1$ [21]	$(2l_{\max} + 1)(4(\alpha_{\max} + k_{\nu}) + 1)$
MIMO - fractional Doppler N_t transmit antennas	$(N_t + 1)(l_{\max} + 1)(2(\alpha_{\max} + k_{\nu}) + 1) - 1$	$((N_t + 1)l_{\max} + N_t)(4(\alpha_{\max} + k_{\nu}) + 1)$

$$\begin{aligned}
y_r[m] &= \sum_{t=1}^{N_t} \sum_{m'=0}^{N-1} \sum_{l'=0}^{l_{\max}} \sum_{j=1}^{P_l} h_{l',j}^{[r,t]} \mathcal{E}(l', \nu_{l',j}, m, m') x_t[m'] + w_r[m], \quad 0 \leq m \leq N-1 \\
&= \underbrace{\sum_{j=1}^{P_l} h_{l,j}^{[r,t]} \mathcal{E}(l, \nu_{l,j}, m, \tilde{m}_t^{\text{pilot}}) x_t^{\text{pilot}}}_{\tilde{\mathbf{H}}_{r,t}[m, \tilde{m}_t^{\text{pilot}}] x_t^{\text{pilot}}} + \underbrace{\sum_{l'=0, l' \neq l}^{l_{\max}} \sum_{j=1}^{P_{l'}} h_{l',j}^{[r,t]} \mathcal{E}(l', \nu_{l',j}, m, \tilde{m}_t^{\text{pilot}}) x_t^{\text{pilot}}}_{\tilde{\mathbf{H}}_{r,t}[m, \tilde{m}_t^{\text{pilot}}] x_t^{\text{pilot}} \text{ (IDI)}} \\
&\quad + \underbrace{\sum_{t'=1, t' \neq t}^{N_t} \sum_{l'=0}^{l_{\max}} \sum_{j=1}^{P_{l'}} h_{l',j}^{[r,t']} \mathcal{E}(l', \nu_{l',j}, m, \tilde{m}_{t'}^{\text{pilot}}) x_{t'}^{\text{pilot}}}_{\text{IPI}} + \underbrace{\sum_{t'=1}^{N_t} \sum_{m'=\tilde{m}_d}^{N-1} \sum_{l'=0}^{l_{\max}} \sum_{j=1}^{P_{l'}} h_{l',j}^{[r,t']} \mathcal{E}(l', \nu_{l',j}, m, m') x_{t'}^{\text{data}}[m'] + w_r[m]}_{\text{IPDI}}.
\end{aligned} \tag{55}$$

given by

$$\begin{aligned}
y_r[m] &= \sum_{t=1}^{N_t} \sum_{m'=\tilde{m}_d}^{N-1} \sum_{l=0}^{l_{\max}} \sum_{j=1}^{P_{l'}} h_{l,j}^{[r,t]} \mathcal{E}(l, \nu_{l,j}, m, m') x_t^{\text{data}}[m'] \\
&\quad + \underbrace{\sum_{t=1}^{N_t} \sum_{l=0}^{l_{\max}} \sum_{j=1}^{P_l} h_{l,j}^{[r,t]} \mathcal{E}(l, \nu_{l,j}, m, \tilde{m}_t^{\text{pilot}}) x_t^{\text{pilot}}}_{\text{IPDI}} + w_r[m].
\end{aligned} \tag{56}$$

We can observe from (56) that, due to the fractional Doppler, the received data symbols are interfered by all the pilots, which can also be alleviated by enlarging k_{ν} for the same reason.

V. ORTHOGONAL RESOURCE ALLOCATION AND CHANNEL ESTIMATION FOR AFDMA SYSTEM

Inspired by the symbol arrangement in EPA-DR channel estimation scheme, we propose a practical and efficient resource allocation scheme for AFDMA system. For ease of illustration, we consider N_U users with single antenna, while the base station (BS) has N_{BS} antennas. Due to space limitations, only the integer Doppler case is presented since the fractional Doppler case can be obtained with some modifications similar to Section IV-B.

Different from the point-to-point MIMO-AFDM system discussed above, the delay-Doppler profiles between the BS and different users are independent of each other. Let $\alpha_{\max}^{[\text{BS}, u]}$ and $l_{\max}^{[\text{BS}, u]}$ denote the maximum Doppler and maximum delay between the BS and the u -th user, respectively, $\tilde{\alpha}_{\max} = \max\{\alpha_{\max}^{[\text{BS}, u]} | u \in [1, N_U]\}$. Then the AFDM parameter c_1 should be set as $\frac{2\tilde{\alpha}_{\max} + 1}{2N}$. Define $L_u \triangleq (l_{\max}^{[\text{BS}, u]} + 1)(2\tilde{\alpha}_{\max} + 1) - 1$, where L_u s satisfy

$$L_1 \leq L_2 \leq \dots \leq L_{N_U} \leq L_{\max}. \tag{57}$$

i.e., the users are sorted in order of value L_u . The parameter L_{\max} is an arbitrary integer that satisfies equation (57). Suppose that the BS is aware of L_{\max} and all the L_u s, while each user only knows L_{\max} and its own L_u .

A. Downlink

In downlink communication, the symbol arrangement at the b -th transmit antenna ($b = 1, \dots, N_{\text{BS}}$) in the BS is

$$x_b[m] = \begin{cases} x_b^{\text{pilot}}, & m = (L_{\max} + 1)t - 1 \\ x_{b,u}^{\text{data}}[m], & m \in \mathbb{D}_u, u = 1, \dots, N_U \\ 0, & \text{otherwise} \end{cases} \tag{58}$$

where x_b^{pilot} is the pilot, \mathbb{D}_u is the resource block allocated to the u -th user for data transmission (each user are assumed to know their own \mathbb{D}_u), $x_{b,u}^{\text{data}}[m]$ s are the corresponding data symbols. Guard symbol blocks (GSB) are inserted among the resource blocks to avoid inter-user interference (IUI). Each pilot should be surrounded by two GSBs with a size no less than L_{N_U} , while the u -th resource block \mathbb{D}_u should be protected by two GSBs with a size no less than L_u . When these conditions are satisfied, all the users can separate their own received data symbols from the others perfectly, making the data detection for each user simpler. An example of AFDMA downlink system with three single-antenna users and a three-antenna BS is presented in Fig. 8⁴.

The pilot and guard overhead for one TA of BS in downlink communication is given by

$$O_{\text{downlink}} = (N_{\text{BS}} + 1)L_{\max} + N_{\text{BS}} + \sum_{u=2}^{N_U} L_u. \tag{59}$$

⁴Although the data symbols for user 1 and user 2 will coincide with each other at user 3, it is acceptable since the target data symbols of user 3 are not contaminated. Moreover, if we shift the orders of \mathbb{D}_2 and \mathbb{D}_3 in Fig. 8, then the GBS with the size of L_2 need to be enlarged to L_3 , i.e., fewer data symbols can be transmitted.

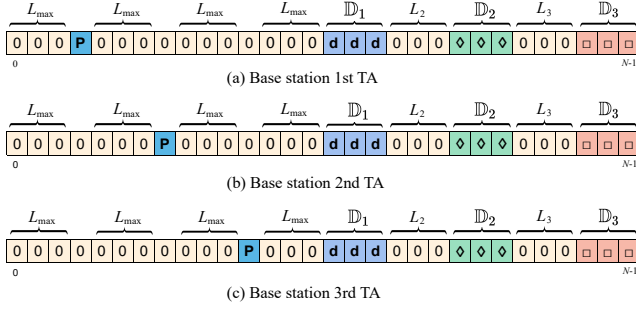


Fig. 8. AFDMA downlink system with three single-antenna users and a three-antenna BS ('P': pilot, '0': guard, 'd': data symbol for the user 1, '◊': data symbol for the user 2, '◻': data symbol for the user 3).

The size of \mathbb{D}_u s ($u = 1, \dots, N_u$) can be tuned flexibly according to the throughput demands of different users, as long as their summation satisfies

$$\sum_{u=1}^{N_u} |\mathbb{D}_u| = N - O_{\text{downlink}}. \quad (60)$$

Based on the symbol arrangement in (58), each user exploits the associated received symbols for EPA-DR channel estimation and data detection.

B. Uplink

We first divide the entire AFDM frame into N_u orthogonal resource blocks as $\mathbb{B}_1, \mathbb{B}_2, \dots, \mathbb{B}_{N_u}$ according to the throughput demands of different users (suppose that the BS is aware of the resource blocks allocation thoroughly, while each user only knows its own resource block \mathbb{B}_u), where $\sum_{u=1}^{N_u} |\mathbb{B}_u| = N$. Then each user arranges its pilot and data block \mathbb{D}_u in its own resource block. Similar to the downlink case, GSBs should be placed appropriately to avoid IUI. An example of AFDMA uplink system with three single-antenna users and a three-antenna BS is presented in Fig. 9. The pilot and guard overhead of the u -th user in uplink communication is $O_{\text{uplink}}^u = 2L_u$.

With the above symbol arrangement, the received symbols corresponding to different users can be separated in the BS perfectly. The BS explores the associated received symbols to perform EPA-DR channel estimation and data detection for each user. Note that in uplink communication, sorting the users in the order of their L_u values is not necessary.

A simpler solution is to replace all the L_u s with L_{\max} roughly in both downlink and uplink communications, and the users ordering in (57) is no longer necessary. However, this simplification will incur spectral efficiency degradation.

The main idea of the above downlink and uplink symbol arrangements is reducing the guard symbols used to ensure orthogonal resource allocation and channel estimation to the greatest extent. It is done by flexibly exploring the differences in the delay-Doppler profiles between the BS and all the users, i.e., the sizes of the non-zero bands of different effective channel matrices. Compared to the orthogonal resource allocation based OTFS-MA system proposed in [18], which suffers from excessive guard symbol overhead due to the 2D structure of

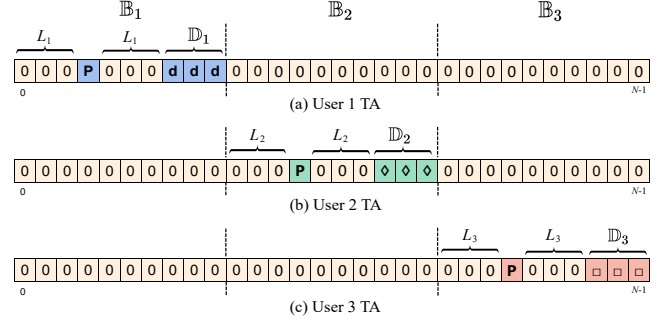


Fig. 9. AFDMA uplink system with three single-antenna users and a three-antenna BS ('P': pilot, '0': guard, 'd': data symbol of the user 1, '◊': data symbol of the user 2, '◻': data symbol of the user 3).

OTFS, the AFDMA system designed above is efficient and easy to implement. Meanwhile, it preserves a large degree of freedom for the BS and users to accommodate various communication requirements. Therefore, we can conclude that AFDMA is a promising solution for multiple access in doubly selective channels.

VI. SIMULATION RESULTS

In this section, we present the performance of MIMO-AFDM in terms of BER with ideal and our estimated CSI. Both integer and fractional Doppler cases are considered. Each transmit antenna transmits independent information symbols.

A. Perfect CSI

Following the vectorized input-output relationship in equation (20), we apply ML detector to verify the diversity analysis in Section III with small frame sizes. In the case of large frame size, MP detector is used since the complexity of ML detector is too high to implement. We assume the channel gains of all paths follow the distribution of $\mathcal{CN}(0, 1/P)$. Other parameters considered for the simulation are provided in Table II.

TABLE II
SIMULATION PARAMETERS FOR PERFECT CSI

Parameter	Value
Carrier frequency f_c (GHz)	4
Subcarrier spacing Δf_{AFDM} (kHz)	2
Maximum UE speed (kmph)	540, 432
Maximum Doppler shift (Hz)	2000, 1600
Number of paths (P)	2, 3 and 5
Modulation scheme	BPSK
Detector	ML, MP

Fig. 10 shows the BER performance of SISO-AFDM and 2×2 MIMO-AFDM systems with integer Doppler. Without losing of generality, we consider $N_{\text{AFDM}} = 6$, $P = 2$ and 3. Asymptotic lines with slopes of 2 ($((\text{SNR})^{-2})$), 3 ($((\text{SNR})^{-3})$), 4 ($((\text{SNR})^{-4})$) and 6 ($((\text{SNR})^{-6})$) are plotted. We can observe that the MIMO-AFDM system outperforms SISO-AFDM system thanks to the space diversity gain from multiple RAs. Meanwhile, the multiple TAs of MIMO-AFDM system bring in the advantages of linear increment in spectral efficiency with the number of TAs. Furthermore, the diversity orders achieved by

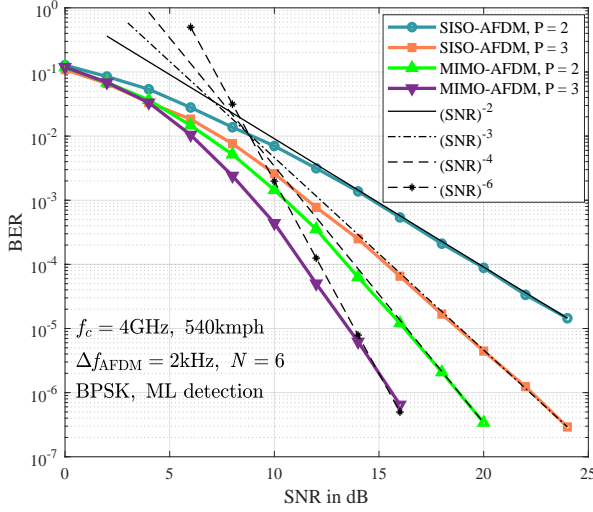


Fig. 10. BER performance of SISO-AFDM and 2×2 MIMO-AFDM systems with integer Doppler. The normalized delay-Doppler profiles (l_i, ν_i) of two paths: (0, 0) and (1, 1); three paths: (0, 0), (0, 1) and (1, 1).

SISO-AFDM in channels with two and three paths are 2 and 3 respectively, while the 2×2 MIMO-AFDM counterparts are 4 and 6 respectively, proving the validity of the diversity order derived in Section III.

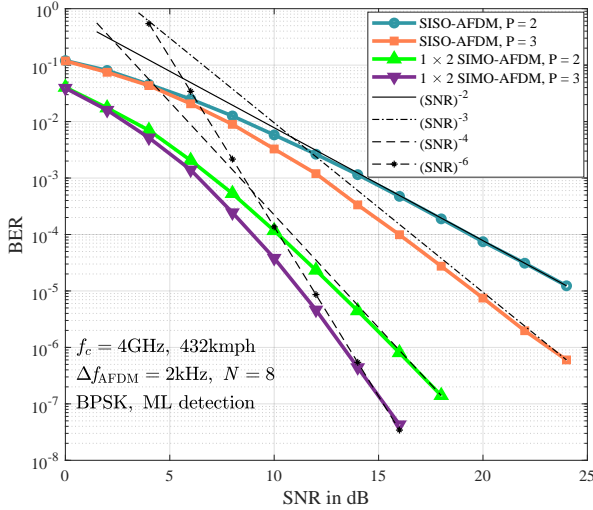


Fig. 11. BER performance of SISO-AFDM and 1×2 SIMO-AFDM systems with fractional Doppler. The normalized delay-Doppler profiles (l_i, ν_i) of two paths: (0, 0) and (1, 0.5); three paths: (0, 0), (0, 0.5) and (1, 0.8).

In Fig. 11, we consider the BER performance of SISO-AFDM and 1×2 SIMO-AFDM systems with fractional Doppler. $N = 8$, $P = 2$ and 3 are adopted. Asymptotic lines with slopes of 2 ($(\text{SNR})^{-2}$), 3 ($(\text{SNR})^{-3}$), 4 ($(\text{SNR})^{-4}$) and 6 ($(\text{SNR})^{-6}$) are provided. We can notice that the diversity orders achieved by SISO-AFDM in channels with two and three paths are 2 and 3 respectively, while the 1×2 SIMO-AFDM counterparts are 4 and 6 respectively, which means the analytical diversity order derived for the integer Doppler case in Section III also holds for the fractional Doppler case, i.e., MIMO-AFDM can achieve full diversity in both integer and fractional Doppler cases.

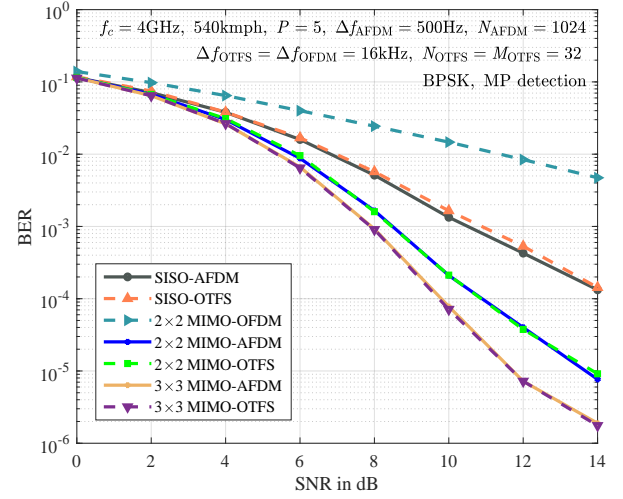


Fig. 12. BER comparisons among SISO-AFDM, SISO-OTFS, MIMO-OFDM, MIMO-AFDM and MIMO-OTFS systems with integer Doppler and $N = 1024$. The normalized delay-Doppler profile of five path: (0, 0), (1, 1), (2, 2), (3, 3), (4, 4).

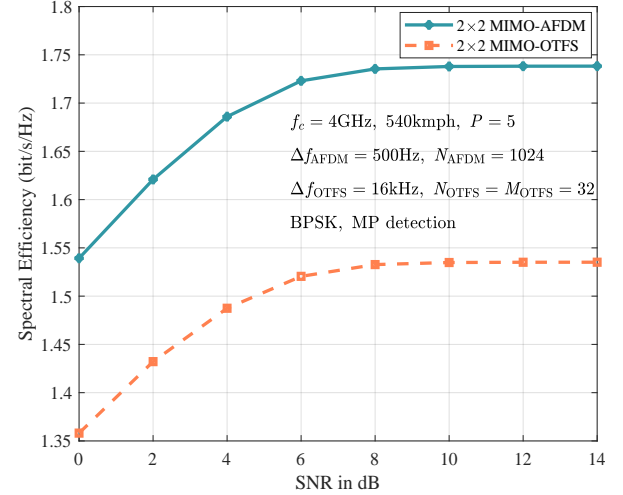


Fig. 13. Spectral efficiency comparison between the 2×2 MIMO-AFDM and the 2×2 MIMO-OTFS systems in Fig. 12.

Fig. 12 shows the BER performance comparisons among SISO-AFDM, SISO-OTFS, MIMO-OFDM, MIMO-AFDM and MIMO-OTFS systems with integer Doppler. Recalling that an OTFS frame with duration $N_{\text{OTFS}}T_{\text{OTFS}}$ (seconds) and bandwidth $M_{\text{OTFS}}\Delta f_{\text{OTFS}}$ (Hz) transmits $N_{\text{OTFS}}M_{\text{OTFS}}$ symbols, where T_{OTFS} and Δf_{OTFS} represent the time and frequency domain sample intervals, respectively, and satisfy $T_{\text{OTFS}}\Delta f_{\text{OTFS}} = 1$; N_{OTFS} and M_{OTFS} denote the number of samples in the time-frequency plane (or Doppler-delay plane)⁵. We adopt $f_c = 4$ GHz, $\Delta f_{\text{AFDM}} = 500$ Hz, $N_{\text{AFDM}} = 1024$, $\Delta f_{\text{OTFS}} = \Delta f_{\text{OFDM}} = 16$ kHz, $N_{\text{OTFS}} = M_{\text{OTFS}} = 32$ to ensure the same resources are occupied. $P = 5$ paths with BPSK and MP detection are applied. We can observe that the 2×2 MIMO-AFDM system outperforms the 2×2 MIMO-OFDM system significantly. This is because MIMO-OFDM suffers from severe inter-carrier interference caused by

⁵For more information about the settings of OTFS, please refer to [6], [7].

the heavy Doppler shifts. Moreover, owing to the equivalent delay-Doppler channel representation in the DAFT domain, AFDM establishes nearly the same BER performance as OTFS in SISO and MIMO configurations with large frame sizes. However, considering the lower overhead of MIMO-AFDM system when conducting the pilot-aided channel estimation, MIMO-AFDM will enjoy higher spectral efficiency than MIMO-OTFS. For example, according to Table I, the pilot and guard overhead of 2×2 MIMO-AFDM for channel estimation is 134 slots, corresponding to 13.08% of the entire AFDM frame, while the 2×2 MIMO-OTFS counterpart is 238 slots, corresponding to 23.24% of the entire OTFS frame. This difference translates into a huge spectral efficiency gap between MIMO-AFDM and MIMO-OTFS, as shown in Fig. 13, where the values of spectral efficiency were calculated from the BER values in Fig. 12.

B. Imperfect CSI

We next apply the EPA-DR scheme for channel estimation and the MP detector for signal detection. $P = 4$ paths with normalized delay profile of $[0, 0, 1, 2]$ are adopted. Each path has a single doppler shift generated by using Jakes' formula, i.e., $\nu_i = \nu_{\max} \cos(\theta_i)$, where θ_i is uniformly distributed over $[-\pi, \pi]$, $\nu_{\max} = 2$ corresponds to a maximum doppler shift of 2000 Hz and a maximum UE speed of 540 kmph. The channel gains of all paths follow the distribution of $\mathcal{CN}(0, 1/P)$. The pilot signal for SNR is denoted as SNRp, while the received data signal for SNR is denoted as SNRd. Other parameters considered for the simulation are provided in Table III.

TABLE III
SIMULATION PARAMETERS FOR IMPERFECT CSI

Parameter	Value
Carrier frequency f_c (GHz)	4
Subcarrier spacing Δf_{AFDM} (kHz)	1
Number of subcarrier (frame size) N_{AFDM}	1024
Maximum UE speed (kmph)	540
Maximum Doppler shift (Hz)	2000
Number of paths (P)	4
Modulation scheme	BPSK
MIMO configuration	2×2
Detector	MP

Fig. 14 shows the BER versus SNRd of MIMO-AFDM with different SNRp in the case of integer Doppler. We can observe that the BER performance enhances as SNRp increases. This is because when we use (39) in **Step 3** of EPA-DR to calculate the $\hat{\mathbf{H}}_{r,t}$, the noise (normalized by x_t^{pilot} in **Step 2** of EPA-DR) contained in the extracted non-zero band will spread over all the other estimated non-zero bands in $\hat{\mathbf{H}}_{r,t}$ simultaneously. Therefore, the larger energy of the pilot, the more accurate of the estimated $\hat{\mathbf{H}}_{r,t}$. Moreover, when SNRp reaches 30 dB, the BER of MIMO-AFDM system using the estimated CSI shows only marginal degradation compared to that with Perfect CSI, which validates the effectiveness of the EPA-DR scheme. Note that in practice, it is feasible to suppose a high SNRp value without violating the average transmit power constraint because the zeros guard symbols will balance the overall transmit energy. In addition, we can notice that, with much

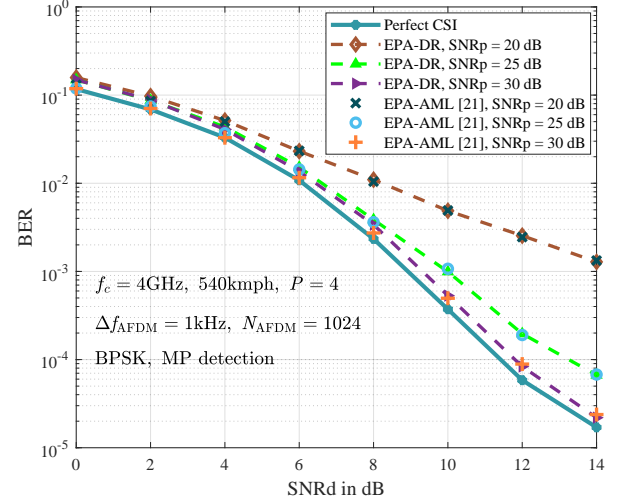


Fig. 14. BER versus SNRd of 2×2 MIMO-AFDM system with different SNRp, integer Doppler.

lower computation complexity, EPA-DR has nearly the same channel estimation performance as EPA-AML.

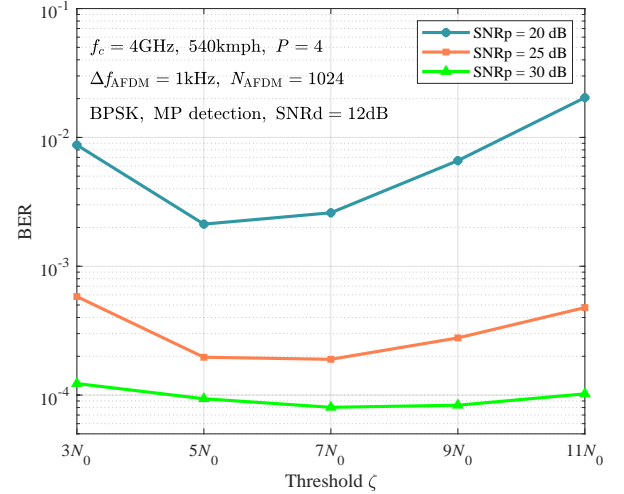


Fig. 15. BER versus different thresholds of 2×2 MIMO-AFDM system, integer Doppler.

Fig. 15 shows the BER versus different thresholds of MIMO-AFDM system with integer Doppler. We set the thresholds by taking N_0 (the variance of noise) as a reference. Three different SNRp values are adopted. We can observe that there exists an optimal threshold for each case. If ζ is set higher than the optimal threshold, the paths with small magnitude channel gain will be omitted; if ζ is set lower than the optimal threshold, the interference of noise with large energy will be enlarged. Both of the cases will deteriorate the accuracy of EPA-DR channel estimation, along with the detection performance degradation. Moreover, we find that with SNRp increasing, the BER performance is less sensitive to the threshold variation, and a larger estimation threshold should be applied to achieve the best BER performance.

We next investigate the effect of spacing factor k_v on the BER performance of MIMO-AFDM system with fractional

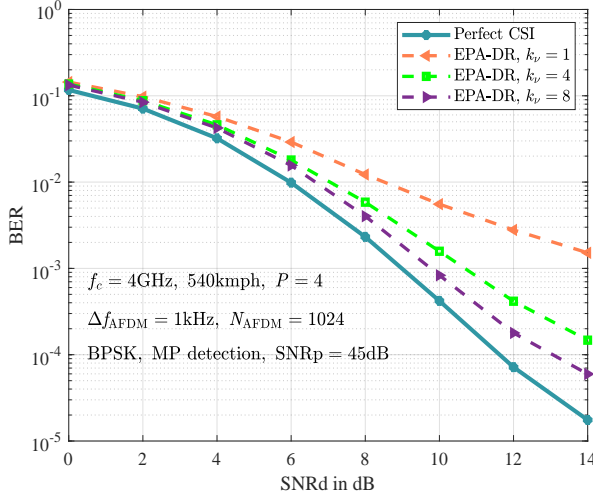


Fig. 16. BER versus SNRd of 2×2 MIMO-AFDM system with different spacing factors k_v , SNRp = 45 dB, fractional Doppler.

Doppler. We simulate three values, $k_v = 1, 4$ and 8 . We can observe that, as k_v increases, the BER performance improves. This is because the protection bands between two contiguous delay blocks in the effective channel matrix are widened, resulting in the contribution of $\tilde{\mathbf{H}}_{\text{eff}}[m, m']$ (defined in (49)) to $\mathbf{H}_{\text{eff}}[m, m']$ being smaller, i.e., the IDI is suppressed. Meanwhile, according to the symbol arrangement in (52), the spacing among all the pilots and the data symbols are also enlarged, leading to the IPI and IPDI being alleviated as well. However, as the k_v increases, the pilot and guard overhead \tilde{O}_{CE} will increase correspondingly (the \tilde{O}_{CE} of the three used k_v values are 62, 116 and 188, respectively, corresponding to 6.05%, 11.33% and 18.40% of the entire AFDM frame), leading to fewer data symbols can be transmitted in each transmit antenna. We can also notice that, compared to the integer Doppler case, a higher SNRp is required with fractional Doppler due to the pilot energy spreading (as illustrated in Fig. 6).

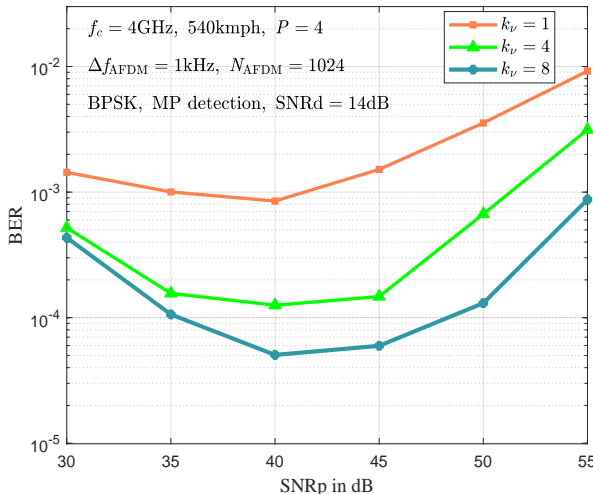


Fig. 17. BER versus SNRp of 2×2 MIMO-AFDM system with different spacing factors k_v , SNRd = 14 dB, fractional Doppler.

Fig. 17 shows the BER versus SNRp of MIMO-AFDM in the case of fractional Doppler. We can observe that, as the SNRp increases, the BER performance first enhances and then degrades. This is because when SNRp is smaller than 40 dB, the noise plays the major role of interference in channel estimation and can be suppressed by enlarging the energy of the pilot. However, according to (56), the IPDI in the received data symbols will be magnified at the same time, making signal detection more difficult even if a more accurate channel estimate is obtained. Therefore, there is a tradeoff between the pilot-aided channel estimation accuracy and the pilot-data symbols separability at the receiver in AFDM with fractional Doppler, which can be interpreted as the cost of compressing the two-dimensional delay-Doppler domain into the one-dimensional DAFT domain.

VII. CONCLUSION

In this paper, we investigate the performance of AFDM with multiple antennas in doubly selective channels for the first time. With ideal CSI, MIMO-AFDM is shown to achieve full diversity, where the full diversity order refers to the number of receive antennas multiplied by the number of resolvable paths. Moreover, MIMO-AFDM is found to establish a BER performance similar to MIMO-OTFS and superior to MIMO-OFDM significantly, while showing a great advantage on spectral efficiency over MIMO-OTFS. Next, by exploring the unique diagonal reconstructability of the AFDM effective channel matrix, we propose a low-complexity channel estimation scheme for MIMO-AFDM. We analyze the induced errors when performing EPA-DR channel estimation in the case of fractional Doppler and find that they can all be suppressed by increasing the spacing factor. Simulation results show that the BER performance of MIMO-AFDM applying EPA-DR channel estimation is very close to the case with ideal CSI. Finally, based on the symbol arrangement in EPA-DR, we propose an orthogonal resource allocation scheme for AFDM system. In the future, space-time coding can be investigated to extract the full transmit diversity in the MIMO-AFDM system. Moreover, pulse-shaping in AFDM can be considered to further study the influence of fractional delay and synchronization effects.

REFERENCES

- [1] J. Wu and P. Fan, "A survey on high mobility wireless communications: challenges, opportunities and solutions," *IEEE Access*, vol. 4, pp. 450-476, 2016.
- [2] F. Hlawatsch and G. Matz, Eds., *Wireless Communications Over Rapidly Time-Varying Channels*. New York, NY, USA: Academic, 2011.
- [3] X. Cai and G. B. Giannakis, "Bounding performance and suppressing intercarrier interference in wireless mobile OFDM," *IEEE Transactions on Communications*, vol. 51, no. 12, pp. 2047-2056, Dec. 2003.
- [4] T. Wang, J. G. Proakis, E. Masry, and J. R. Zeidler, "Performance degradation of OFDM systems due to doppler spreading," *IEEE Transactions on Wireless Communications*, vol. 5, no. 6, pp. 1422-1432, 2006.
- [5] T. Hwang, C. Yang, G. Wu, S. Li, and G. Ye Li, "OFDM and its wireless applications: A survey," *IEEE Transactions on Vehicular Technology*, vol. 58, no. 4, pp. 1673-1694, May 2009.
- [6] R. Hadani, S. Rakib, M. Tsatsanis, A. Monk, A. J. Goldsmith, A. F. Molisch, and R. Calderbank, "Orthogonal time frequency space modulation," *IEEE Wireless Communications and Networking Conference (WCNC)*, pp. 1-6, 2017.

- [7] A. Monk, R. Hadani, M. Tsatsanis, S. Rakib, "OTFS - orthogonal time frequency space: a novel modulation technique meeting 5G high mobility and massive MIMO challenges," *arXiv preprint arXiv:1608.02993*, 2016.
- [8] P. Raviteja, Y. Hong, E. Viterbo, and E. Biglieri, "Effective diversity of OTFS modulation," *IEEE Wireless Communications Letters*, vol. 9, no. 2, pp. 249-253, Feb. 2020.
- [9] S. K. Mohammed, "Derivation of OTFS modulation from first principles," *IEEE Transactions on Vehicular Technology*, vol. 70, no. 8, pp. 7619-7636, Aug. 2021.
- [10] W. Anwar, A. Krause, A. Kumar, N. Franchi, and G. P. Fettweis, "Performance analysis of various waveforms and coding schemes in V2X communication scenarios," *IEEE Wireless Communications and Networking Conference (WCNC)*, pp. 1-8, 2020.
- [11] A. Rezaeadeh, R. A. Farhang, M. Ji, R. R. Chen and B. Farhang Boroujeny, "Analysis of discrete-time MIMO OFDM-based orthogonal time frequency space modulation," *IEEE International Conference on Communications (ICC)*, pp. 1-6, 2018.
- [12] M. K. Ramachandran and A. Chockalingam, "MIMO-OTFS in high-doppler fading channels: signal detection and channel estimation," *IEEE Global Communications Conference (GLOBECOM)*, pp. 206-212, 2018.
- [13] G. D. Surabhi, R. M. Augustine, and A. Chockalingam, "On the diversity of uncoded OTFS modulation in doubly-dispersive channels," *IEEE Transactions on Wireless Communications*, vol. 18, no. 6, pp. 3049-3063, Jun. 2019.
- [14] P. Raviteja, K. T. Phan, and Y. Hong, "Embedded pilot-aided channel estimation for OTFS in delay-doppler channels," *IEEE Transactions on Vehicular Technology*, vol. 68, no. 5, pp. 4906-4917, 2019.
- [15] W. Shen, L. Dai, J. An, P. Fan and R. W. Heath, "Channel estimation for orthogonal time frequency space (OTFS) massive MIMO," *IEEE Transactions on Signal Processing*, vol. 67, no. 16, pp. 4204-4217, Aug. 2019.
- [16] Z. Ni, J. A. Zhang, X. Huang, K. Yang and J. Yuan, "Uplink sensing in perceptive mobile networks with asynchronous transceivers," *IEEE Transactions on Signal Processing*, vol. 69, pp. 1287-1300, 2021.
- [17] Y. Hong, T. Thaj, and E. Viterbo, *Delay Doppler Communications: Principles and Applications*. Elsevier, 2022.
- [18] S. Rakib and R. Hadani, "Multiple access in wireless telecommunications system for high-mobility applications," *US Patent No. US9722741B1*, Aug. 2017.
- [19] V. Khammammetti and S. K. Mohammed, "OTFS-based multiple-access in high doppler and delay spread wireless channels," *IEEE Wireless Communications Letters*, vol. 8, no. 2, pp. 528-531, April 2019.
- [20] G. Surabhi, R. M. Augustine, and A. Chockalingam, "Multiple access in the delay doppler domain using OTFS modulation," *arXiv preprint arXiv:1902.03415*, 2019.
- [21] A. Bemani, N. Ksairi and M. Kountouris, "Affine frequency division multiplexing for next generation wireless communications," *arXiv preprint arXiv:2204.12798*, 2022.
- [22] A. Bemani, N. Ksairi and M. Kountouris, "AFDM: A full diversity next generation waveform for high mobility communications," *IEEE International Conference on Communications Workshops (ICC Workshops)*, pp. 1-6, 2021.
- [23] S. Chang Pei and J. Jiu Ding, "Closed-form discrete fractional and affine fourier transforms," *IEEE Transactions on Signal Processing*, vol. 48, no. 5, pp. 1338-1353, May 2000.
- [24] T. Erseghe, N. Laurenti, and V. Cellini, "A multicarrier architecture based upon the affine fourier transform," *IEEE Transactions on Communications*, vol. 53, no. 5, pp. 853-862, May 2005.
- [25] D. Stojanović, I. Djurović, and B. R. Vojcic, "Multicarrier communications based on the affine fourier transform in doubly-dispersive channels," *EURASIP Journal on Wireless Communications and Networking*, vol. 2010, pp. 1-10, 2010.
- [26] X. Ouyang and J. Zhao, "Orthogonal chirp division multiplexing," *IEEE Transactions on Communications*, vol. 64, no. 9, pp. 3946-3957, Sept. 2016.
- [27] H. Yin, Y. Tang, "Pilot aided channel estimation for AFDM in doubly dispersive channels," *IEEE/CIC International Conference on Communications in China (ICCC)*, pp. 308-313, 2022.
- [28] A. Bemani, N. Ksairi and M. Kountouris, "Low complexity equalization for AFDM In doubly dispersive channels," *IEEE International Conference on Acoustics, Speech and Signal Processing (ICASSP)*, pp. 5273-5277, 2022.
- [29] A. Bemani, G. Cuoizzo, N. Ksairi and M. Kountouris, "Affine frequency division multiplexing for next-generation wireless networks," *International Symposium on Wireless Communication Systems (ISWCS)*, pp. 1-6, 2021.
- [30] Q. Wang, A. Kakkavas, X. Gong and R. A. Stirling-Gallacher, "Towards integrated sensing and communications for 6G," *2nd IEEE International Symposium on Joint Communications & Sensing (JC&S)*, pp. 1-6, 2022.
- [31] Y. Ni, Z. Wang, P. Yuan and Q. Huang, "An AFDM-based integrated sensing and communications," *International Symposium on Wireless Communication Systems (ISWCS)*, pp. 1-6, 2022.
- [32] Z. Wei, W. Yuan, S. Li, J. Yuan and D. W. K. Ng, "Off-grid channel estimation with sparse bayesian learning for OTFS systems," *IEEE Transactions on Wireless Communications*, vol. 21, no. 9, pp. 7407-7426, Sept. 2022.
- [33] P. Raviteja, K. T. Phan, Y. Hong, and E. Viterbo, "Interference cancellation and iterative detection for orthogonal time frequency space modulation," *IEEE Transactions on Wireless Communications*, vol. 17, no. 10, pp. 6501-6515, Oct. 2018.
- [34] W. Yuan, Z. Wei, J. Yuan and D. W. K. Ng, "A simple variational bayes detector for orthogonal time frequency space (OTFS) modulation," *IEEE Transactions on Vehicular Technology*, vol. 69, no. 7, pp. 7976-7980, July 2020.
- [35] T. Thaj and E. Viterbo, "Low complexity iterative rake decision feedback equalizer for zero-padded OTFS systems," *IEEE Transactions on Vehicular Technology*, vol. 69, no. 12, pp. 15 606-15 622, Dec. 2020.
- [36] D. Tse and P. Viswanath, *Fundamentals of Wireless Communication*. Cambridge, U.K.: Cambridge University Press, 2005.